HHS Public Access

Author manuscript

Nat Immunol. Author manuscript; available in PMC 2024 May 13.

Published in final edited form as:

Nat Immunol. 2024 May ; 25(5): 860–872. doi:10.1038/s41590-024-01807-y.

PU.1 and BCL11B sequentially cooperate with RUNX1 to anchor mSWI/SNF to poise the T cell effector landscape

Noah Gamble[1,2,14], **Alexandra Bradu**[1,14], **Jason A. Caldwell**[1,14], **Joshua McKeever**[1,3], **Olubusayo Bolonduro**[1,4], **Ebru Ermis**[1], **Caroline Kaiser**[1,5], **YeEun Kim**[6,7], **Benjamin Parks**[7,8], **Sandy Klemm**[7], **William J. Greenleaf**[8,9,10], **Gerald R. Crabtree**[11,12], **Andrew S. Koh**[1,13,*]

[1]Department of Pathology, University of Chicago, Chicago, IL, USA

[2]Graduate Program in Biophysical Sciences, University of Chicago, Chicago, IL, USA

[3]Committee on Molecular Metabolism and Nutrition, University of Chicago, Chicago, IL, USA

[4]Committee on Genetics, Genomics, Systems Biology, University of Chicago, Chicago, IL, USA

[5]Department of Human Genetics, University of Chicago, Chicago, IL, USA

[6]Immunology Program, Stanford University, Stanford, CA, USA

[7]Department of Genetics, Stanford University, Stanford, CA, USA

[8]Department of Computer Science, Stanford University, Stanford, CA, USA

[9]Department of Applied Physics, Stanford University, Stanford, CA, USA

[10]Chan Zuckerberg Biohub, San Francisco, CA, USA

[11]Department of Pathology, Stanford University, Stanford, CA, USA

[12]Department of Developmental Biology, Stanford University, Stanford, CA, USA

[13]Institute for Biophysical Dynamics, University of Chicago, Chicago, IL, USA

[14]These authors contributed equally

Abstract

Adaptive immunity relies on specialized effector functions elicited by lymphocytes, yet how antigen recognition activates appropriate effector responses through non-specific signaling intermediates is unclear. Here, we examined the role of chromatin priming in specifying the functional outputs of effector T cells and found that most of the *cis*-regulatory landscape active in effector T cells was poised early in development, prior to the expression of the T cell

*Correspondence: akoh@uchicago.edu.

AUTHOR CONTRIBUTIONS

A.S.K. and G.R.C. conceived the study. A.S.K., N.G., A.B., J.A.C., J.M., O.B., E.E., C.K., Y.K. and B.P. conducted experiments. A.S.K., N.G., A.B. and E.E. performed bioinformatic analyses. A.S.K. supervised all experiments and analyses. S.K. and W.J.G. provided resources and conceptual insights. A.S.K. wrote the manuscript with support from N.G., A.B. and J.A.C. All authors reviewed and provided comments on the manuscript.

DECLARATION OF INTERESTS

G.R.C. is a founder and stockholder in Foghorn Therapeutics. W.J.G. is a consultant and equity holder for 10X Genomics, Guardant Health, Quantapore and Ultima Genomics. W.J.G. is a co-founder of Protillion Biosciences and named on patents describing ATAC-seq. The other authors declare no conflict of interest.

antigen receptor. We identified two principal mechanisms underpinning this poised landscape: the recruitment of the nucleosome remodeler mSWI/SNF by the transcription factors RUNX1 and PU.1 to establish chromatin accessibility at T effector loci; and a ‘relay’ whereby the transcription factor BCL11B succeeded PU.1 to maintain occupancy of the chromatin remodeling complex mSWI/SNF together with RUNX1, after PU.1 silencing during lineage commitment. These mechanisms define modes by which T cells acquire the potential to elicit specialized effector functions early in their ontogeny and underscore the importance of integrating extrinsic cues to the developmentally specified intrinsic program.

T cells sense diverse stimuli and elicit specific effector functions to coordinate the adaptive immune response[1, 2]. This coordination is dependent on the T cell antigen receptor (TCR), but how specific information sensed by the TCR is transduced to activate T cell-specific effector programs remains to be clearly defined. A common view to explain the specificity of the effector T cell program postulates an instructive role for the antigen receptor, supported by the impact of TCR signal strength on the phenotypic outcomes of T cell differentiation[3, 4, 5] and the changes in epigenomic states following TCR triggering[6, 7, 8].

However, this receptor-centric view is not sufficient to explain how the same signaling pathways triggered by the TCR activate fundamentally different effector programs in other immune cell types[9, 10], nor is it consistent with the results of ‘receptor-switch’ experiments in which a neuronal muscarinic subtype-1 receptor elicited T cell-specific effector activity in response to its agonist carbachol in T cells without surface TCR[11]. Furthermore, the large overlap between TCR-induced and B cell antigen receptor (BCR)-induced chromatin accessibility[12] suggests the epigenomic remodeling that follows antigen receptor triggering directs shared features of lymphocyte activation[13]. Together these findings suggest the potential to elicit T cell effector functions might be specified prior to antigen receptor signaling and underscore the importance of a developmentally preconditioned program that constrains the range of genomic sites that can be targeted by signaling pathways[14, 15]. The extent of this preconditioning, when it is first established in development and how it is propagated through T cell maturation is largely unknown.

In this study, we traced the chromatin accessibility profiles distinctive to effector T cells back through T cell development and found that the majority of T effector loci became accessible prior to antigen receptor expression. We identified the transcription factor RUNX1 and the chromatin remodeling complex mSWI/SNF as determinants that were necessary but insufficient to establish and maintain accessibility at T cell effector loci. We found that cooperativity between RUNX1 and the transcription factor PU.1 facilitated mSWI/SNF localization at T effector loci in thymic immigrants. We further defined a ‘relay’ whereby the transcription factor BCL11B succeeded PU.1 to maintain RUNX1-mSWI/SNF occupancy at T effector loci and propagate chromatin accessibility at these sites. Taken together, these results define the molecular mechanisms by which T cells acquire the potential to elicit specialized effector functions early in their ontogeny.

RESULTS

Accessibility at many T effector loci precedes TCR expression

To determine when and how T cells acquire the potential to elicit lineage-specific effector activity, we first defined 'T effector loci' (hereafter T_{EFF} loci) by profiling chromatin accessibility landscapes of differentiated $CD8^+$ T cells (terminal $KLRG1^+CD127^-$LCMV-d7-specific effector T cells (T_{EFF} cells), long-lived $CD44^+CD62L^+$LCMV-d180-specific central memory T cells (T_{CM} cells), lung intravenous$^-CD44^+$influenza-d35-specific resident memory T cells (T_{RM} cells), *in vitro* CD3ε/CD28 Ab-treated T_{EFF} cells) and $CD4^+$ T cells (IL-12/IL-4-Ab-treated T_H1 cells, IL-4/IFNγ-Ab-treated T_H2 cells, IL-17A-GFP^+ T_H17 cells from ileum or inflamed brain/spinal cord, $CXCR5^+SLAM^{lo/int}$ T_{FH} cells) using published ATAC-seq[16] (assay for transposase-accessible chromatin) datasets[17, 18, 19, 20, 21]; excluding accessible regions that overlapped those in published ATAC-seq profiles[22] of activated B cells (72h post-lipopolysaccharide/IL-4 treatment) to remove constitutively accessible peaks and those encoding general features of lymphocyte activation[12]; and clustering the remaining peaks into a non-overlapping set representing the unique landscapes of each T_{EFF} cell subtype (Fig. 1a). To link these landscapes to distinctive functional responses, we profiled the transcriptomes of each T_{EFF} cell using RNA-seq datasets from the same samples used to generate the ATAC-seq data[17, 18, 19, 20, 21, 23]. We clustered the transcriptomes (Extended Data Fig. 1a) and found the genes in closest proximity to the subtype-specific ATAC-seq peaks (median distance ~15 kb, Extended Data Fig. 1b) were selectively enriched for genes differentially expressed by the same T_{EFF} cell subtype (Extended Data Fig. 1c). The chromatin landscape of the lung $CD8^+$ T_{RM} cells was the only exception, showing enrichment for genes of many T_{EFF} cell subtypes, e.g. *Ifng*, *Ccr4*, *Rora*, *Bcl6*, *Cxcr3* (Extended Data Fig. 1c). Thus, the defined T_{EFF} loci reflected the distinctive chromatin landscapes and associated gene signatures of the major T cell subtypes.

To identify when T_{EFF} loci first became accessible, we performed ATAC-seq at major stages of T cell development beginning with Lin^- ($NK1.1^-γδTCR^-CD11b^-CD19^-Gr\text{-}1^-CD11c^-Ter119^-$) c-$Kit^{hi}CD25^-CD4^-CD8α^-$ early T lineage progenitors (ETPs), Lin^-c-$Kit^{hi}CD25^{hi}CD4^-CD8α^-$ DN2a and Lin^-c-$Kit^-CD25^{hi}CD4^-CD8α^-$ DN3 thymocytes (Extended Data Fig. 1d-h) to $CD8^+$ or $CD4^+$ $CD19^-γδTCR^-TCRβ^{hi}CD44^{lo}CD62L^{hi}$ naïve T cells (T_N cells). These markers were used to sort the respective lineages throughout this report. We also profiled the accessibility landscapes of serum+LIF (leukemia inhibitory factor)-maintained embryonic stem cells (ESCs), Lin^-CD127^-c-$Kit^{hi}Sca\text{-}1^+Flt3^-$ hematopoietic stem cells (HSCs), Lin^-CD127^-c-$Kit^{hi}Sca\text{-}1^+Flt3^+$ multipotent progenitors (MPPs) and Lin^-CD127^+c-$Kit^{hi}Sca\text{-}1^+Flt3^+$ common lymphoid progenitors (CLPs) using published ATAC-seq datasets[8, 24]. These profiles showed that a large fraction ($\bar{x}$ = 71.2 %) of T_{EFF} loci first became accessible in the thymus (Fig. 1b-d and Extended Data Fig. 1i), with the greatest gain in *de novo* accessibility ($\bar{x}$ = 19.2 % of T_{EFF} loci) in ETPs (Fig. 1b-d and Extended Data Fig. 2a-f), with nearly half of all T_{EFF} loci, including *Prf1*, *Gzmb* and *Ifng*, accessible by the DN2a stage (Fig. 1b-d and Extended Data Fig. 1i, 2a-f). The regions in which accessibility was established in ETP-DN3 thymocytes overlapped with the accessible genomes of a median of 2 (75 percentile=5) of the 23 T effector samples we profiled (Fig. 1e and Extended Data Fig. 2g-l), which was less

than that for ESC-established (median=5, 75 percentile=9) or HSC/MPP/CLP-established peaks (median=4, 75 percentile=9), indicating a greater enrichment for subtype-specific T_{EFF} loci (e.g. *Tbx21, Il4*, *Il17a* and *Icos*) compared to more common T_{EFF} loci (e.g. *Cd69*, *Cd40lg*) (Fig. 1c,e and Extended Data Fig. 2g-l). The poising of these T_{EFF} loci was not affected by treatment with FK506, an inhibitor of calcineurin that blocks the calcium-NFAT signaling pathway – a key arm of TCR signal transduction[25] (Extended Data Fig. 3a,b) – indicating that most chromatin accessibility at T_{EFF} loci was independent of TCR signaling.

Enhancer priming mediates early accessibility at T_{EFF} loci

To test whether the accessibility at T_{EFF} loci in DN thymocytes reflected active transcription needed for early T cell development, we profiled the transcriptomes of ETP-DN3 thymocytes using published RNA-seq datasets[23] and assessed the expression levels of genes neighboring the T_{EFF} loci (T_{EFF} genes). The large majority (>80%) of T_{EFF} genes were transcriptionally silent or expressed at levels orders of magnitude lower than those in effector T cells (Fig. 1c, Extended Data Fig. 1i, 4a,b). We further characterized these loci by profiling the state of histone modifications and RNA polymerase II (POL II) occupancy using published chromatin immunoprecipitation (ChIP-seq) and global run-on (GRO-seq) sequencing datasets[26, 27]. We found an enrichment of H3K4me1 and depletion of H3K27ac, H3K4me3 and POL II, cardinal features of transcriptionally inactive distal enhancers[28] (Extended Data Fig. 4c), consistent with ~83% of T_{EFF} loci being gene-distal (Extended Data Fig. 4d). These data indicated that the accessibility at T_{EFF} loci in early thymocyte subsets largely reflected enhancer priming[28, 29].

Distinct regulatory logic underlies early poising at T_{EFF} loci

Next, we sought to identify potential transcription factors that could be targeting these regions in early T cell development by conducting transcription factor motif enrichment analysis within accessible T_{EFF} loci specific to $CD8^+$ T_{EFF}, $CD4^+$ T_H1, $CD4^+$ T_H2, $CD4^+$ T_H17 and $CD4^+$ T_{FH} cells in ESCs, HSCs, MPPs, CLPs, ETP, DN2a and DN3 thymocytes using the same ATAC-seq profiles generated above. We found a sharp enrichment of ETS and RUNX motifs at the ETP-DN3 stages at all assessed T_{EFF} loci (compared to ESC-CLPs), and a more modest enrichment of AP-1 motifs in ETP-DN3 stages at accessible loci specific for $CD4^+$ T_H1, $CD4^+$ T_H2 and $CD4^+$ T_H17 cells compared to those specific for $CD8^+$ T_{EFF} cells or $CD4^+$ T_{FH} cells (Fig. 2a). Motifs for STAT factors (e.g. STAT3, STAT4, STAT5) were enriched in DN2a-DN3 thymocytes at accessible loci specific for $CD4^+$ T_H2 cells and $CD8^+$ T_{EFF} cells (Fig. 2a). Using published ChIP-seq datasets[30, 31, 32, 33, 34, 35, 36, 37], we detected robust localization of AP-1 and STAT factors, as well as NFAT and NF-κB, at T_{EFF} loci poised at ETP-DN3 stages in activated $CD4^+$ T_H1 cells, $CD4^+$ T_H17 cells and $CD8^+$ T_{EFF} cells (Extended Data Fig. 5a-e), suggesting that accessibility at these early stages of T cell development may specify the genomic regions that signal-regulated transcription factors could later target upon TCR and cytokine receptor signaling.

We next used the STRING database (string-d.org) to generate a network of known and predicted protein-protein interactions between the top decile of transcription factors from our motif enrichment analysis and subunits of the major cofactor complexes attributed to promoting *de novo* chromatin accessibility[28, 29, 38], such as the trithorax group complexes

mSWI/SNF (also known as BAF) chromatin remodeling complex and COMPASS histone methyltransferase complex. We observed a strong bias of interactions between the transcription factors and subunits of the mSWI/SNF complex, an antagonist of Polycomb repression[38] (Fig. 2b). Aggregate density analysis of published H3K27me3 ChIP-seq[39] read dyads indicated focal depletion of H3K27me3 at T_{EFF} loci compared to other accessible regions of the genome in ETP–DN2b thymocytes (Fig. 2c), consistent with the eviction of Polycomb following recruitment of mSWI/SNF to T_{EFF} loci.

To test the functional role of mSWI/SNF in the early poising of T_{EFF} loci, we generated *Smarca4*$^{f/f}$*Rosa*$^{CreERT2/nTnG}$ mice, in which tamoxifen treatment induces deletion of the gene encoding the mSWI/SNF ATPase SMARCA4, also known as BRG1. We sorted and cultured *Smarca4*$^{f/f}$*Rosa*$^{CreERT2/nTnG}$ Lin^{-}Sca-1^{+}c-Kit^{+} (hereafter LSK) hematopoietic progenitors on OP9-DL4[40] (Extended Data Fig. 6a) and treated with tamoxifen or ethanol at day 4 of culture (30h), washed out, replated and sorted GFP^{+} KO (hereafter SMARCA4 cKO) or tdTomato^{+} WT (hereafter SMARCA4 WT) ETP, DN2a or DN3 thymocytes at day 8 for ATAC-seq (Extended Data Fig. 6b). GFP^{+} SMARCA4 cKO cells were outcompeted by tdTomato^{+} cells in the same tamoxifen-treated culture (Extended Data Fig. 6b), suggesting a fitness loss in SMARCA4 cKO cells. However, the ratio of ETP:DN2a:DN3 thymocytes was comparable between SMARCA4 cKO and SMARCA4 WT thymocytes in the OP9-DL4 co-cultures (Extended Data Fig. 6b), suggesting the developmental heterogeneity of cells at the time of tamoxifen treatment yielded asynchronously differentiating SMARCA4 cKO cells to reach respective ETP, DN2a and DN3 stages prior to depletion of SMARCA4 levels. We found significant decreases in chromatin accessibility at 5,209, 10,743 and 10,415 T_{EFF} loci in SMARCA4 cKO compared to SMARCA4 WT ETP, DN2a and DN3 thymocytes, respectively (Fig. 2d). Furthermore, the *de novo* gain in ATAC-seq fragment density at T_{EFF} loci established in SMARCA4 WT ETPs was substantially diminished at 74.6% and 70.5% of these loci in SMARCA4 cKO DN2a and DN3 thymocytes, respectively (Fig. 2e,f). Likewise, the *de novo* accessibility at T_{EFF} loci established in SMARCA4 WT DN2a thymocytes became diminished in 80.9% of SMARCA4 cKO DN3 thymocytes (Fig. 2e,f). These results indicated that SMARCA4 had a critical role in the establishment and maintenance of chromatin accessibility at T_{EFF} loci in early T cell development.

To determine whether the loci dependent on SMARCA4 for chromatin accessibility in ETP-DN3 thymocytes (Extended Data Fig. 6c) were directly bound by mSWI/SNF, we performed CUT&RUN (cleavage under targets & release using nuclease)[41] for BAF155, a core subunit of mSWI/SNF, in sorted Lin^{-}CD25^{+}CD4^{-}CD8^{-} DN2-DN3 thymocytes (hereafter DN2-DN3) differentiated from wild-type mouse LSK progenitors on OP9-DL4 cultures. We found BAF155 CUT&RUN fragment density selectively enriched at T_{EFF} loci compared to accessible regions that were not T_{EFF} loci in wild-type DN2-DN3 thymocytes (Extended Data Fig. 6d). Moreover, we found robust mSWI/SNF occupancy at 82.8% of SMARCA4-induced ETP-DN3 established T_{EFF} loci compared to that at background regions ±2 kb of these loci (Fig. 2e,f, Extended Data Fig. 6c). Of note, the changes in chromatin accessibility at T_{EFF} loci in SMARCA4 cKO ETP-DN3 thymocytes did not correlate with local mRNA expression from the associated genes, as the large majority (~86–89%) of the T_{EFF} loci were associated with transcriptionally inactive genes (Extended Data Fig. 4a) and less than 1% of the transcribed T_{EFF} loci (~11-14% of total T_{EFF} loci) were downregulated in SMARCA4

cKO compared to SMARCA4 WT ETP-DN3 thymocytes (Extended Data Fig. 6e,f). Taken together, these data indicated that mSWI/SNF was a positive regulator of chromatin poising at T_{EFF} loci in early T cell development.

RUNX1 facilitates mSWI/SNF recruitment to poise T_{EFF} loci

To identify the specific transcription factors that interacted with mSWI/SNF to establish and maintain accessibility at T_{EFF} loci in early T cell development, we leveraged the ATAC-seq data from SMARCA4 cKO ETP-DN3 thymocytes to distinguish the motif lexicon of SMARCA4-induced versus SMARCA4-independent T_{EFF} loci. We found significant enrichment of binding motifs for ETS and RUNX factors at an order of magnitude greater than that for CTCF motifs within SMARCA4-induced regions (e.g. *Prf1*, *Il2*, *Icos*) in ETP-DN3 thymocytes. In contrast, SMARCA4-independent sites (e.g. *Klrg1*, *Ccr4*, *Sell*) were significantly enriched for CTCF motifs at an order of magnitude greater than that for ETS and RUNX motifs (Fig. 3a). Because half of all transcription factor-mSWI/SNF associations in the above STRING-generated protein interaction network was connected to RUNX1, we focused on RUNX1 as a potential mSWI/SNF targeting factor. Using published ChIP-seq datasets[27, 42], we investigated whether RUNX1 bound to the same T_{EFF} loci that mSWI/SNF regulated in ETP-DN3 thymocytes. We found focal RUNX1 occupancy at 87.2% and 85.9% of SMARCA4-induced T_{EFF} loci in ETPs and DN2-DN3 thymocytes, respectively, with enhanced RUNX1, but not CTCF ChIP-seq[26] read density at these sites compared to SMARCA4-independent T_{EFF} loci (Fig. 3b), indicating preferential localization of RUNX1 at SMARCA4-induced sites in ETP-DN3 thymocytes. Leveraging the ETP-DN3 SMARCA4 WT and SMARCA4 cKO ATAC-seq datasets, we assessed differences in transcription factor footprinting at T_{EFF} loci with RUNX1 motifs (e.g. *Ifng*, *Il2*, *Icos*). We found the difference in Tn5 insert density between the center and flanking regions of the RUNX1 motif (footprint depth) was substantially diminished by 29.9%, 24.2% and 39.1% in SMARCA4 cKO compared to SMARCA4 WT ETPs, DN2a and DN3 thymocytes, respectively (Fig. 3c). By contrast, no change in footprint depth was detected at the CTCF motif at the same stages (Fig. 3c), indicating synergy between RUNX1 and mSWI/SNF co-occupancy at SMARCA4-induced T_{EFF} loci in early thymocyte progenitors.

To test whether mSWI/SNF localization at T_{EFF} loci in ETP-DN3 thymocytes depended on RUNX1, we generated $Runx1^{f/f}Rosa^{CreERT2/nTnG}$ mice, cultured sorted LSK progenitors on OP9-DL4, treated them with tamoxifen or ethanol at day 4, washed out, replated and sorted GFP^+ cells (hereafter RUNX1 cKO) or $tdTomato^+$ cells (hereafter RUNX1 WT) ETPs at day 8 (Extended Data Fig. 7a). BAF155 CUT&RUN in RUNX1 cKO ETPs and pooled DN2-DN3 thymocytes indicated a marked loss of mSWI/SNF localization at T_{EFF} loci compared to RUNX1 WT ETP and DN2-DN3 thymocytes (Fig. 3d), with a more pronounced loss of BAF155 occupancy at SMARCA4-induced compared to SMARCA4-independent T_{EFF} loci (Fig. 3d), suggesting that RUNX1 was required for recruitment of mSWI/SNF to T_{EFF} loci in ETP-DN3 thymocytes. To determine whether the loss in mSWI/SNF targeting due to *Runx1* deletion impacted chromatin accessibility at T_{EFF} loci, we performed ATAC-seq on sorted RUNX1 cKO and RUNX1 WT ETP, DN2a and DN3 thymocytes and found 74.2%, 82.0% and 81.3% of SMARCA4-induced loci (e.g. *Icos*, *Ifng*) exhibited decreased chromatin accessibility in RUNX1 cKO compared to RUNX1 WT ETPs-DN3 (Fig. 3e-

h), indicating strong synergy between RUNX1 and SMARCA4 in establishing chromatin accessibility at T_{EFF} loci. The mRNA levels at <1% of transcriptionally active T_{EFF} loci were downregulated in RUNX1 cKO compared to RUNX1 WT ETP-DN3 thymocytes (Extended Data Fig. 7b-g), indicating that changes in chromatin accessibility at the RUNX1-induced T_{EFF} loci were not caused by changes in local gene expression. Together, these results showed that RUNX1 and mSWI/SNF cooperated to facilitate the induction of *de novo* accessibility at T_{EFF} loci in early T cell development.

BCL11B maintains poising at SMARCA4-induced T_{EFF} loci

mSWI/SNF complexes assemble lineage-specific combinations of subunits to impart unique biological functions across different tissues[43]. BCL11B, a major determinant of T lineage commitment whose expression is induced at the DN2a stage[44, 45, 46] is the only putative T cell-specific mSWI/SNF complex subunit reported to date[47]. To investigate whether BCL11B contributed to imparting T cell-specific mSWI/SNF function that promoted chromatin accessibility at T_{EFF} loci in early T cell development, we profiled the genomic occupancy of BCL11B in sorted wild-type mouse DN2-DN3 thymocytes using published ChIP-seq datasets[27]. We found robust BCL11B occupancy at 82.8% of SMARCA4-induced, ETP-DN3 established T_{EFF} loci in DN2-DN3 thymocytes compared to that at background regions ±2 kb of these loci (Fig. 4a,b). Furthermore, we found enhanced focal BCL11B ChIP-seq read density at mSWI/SNF-localized, SMARCA4-induced T_{EFF} loci compared to that at SMARCA4-independent T_{EFF} loci (Fig. 4a,b). To determine whether this preferential localization had functional consequences, we generated *Vav1-iCre*$^{+}$*Bcl11b*$^{f/f}$ mice and performed ATAC-seq on sorted DN2a and separately sorted DN3 thymocytes from *Vav1-iCre*$^{+}$*Bcl11b*$^{f/f}$ mice (hereafter BCL11B cKO) and *Vav1-iCre*$^{-}$*Bcl11b*$^{f/f}$ sex-matched littermates (hereafter BCL11B WT) (Extended Data Fig. 8a). 70.7% and 54.6% of SMARCA4-induced T_{EFF} loci had diminished chromatin accessibility in BCL11B cKO compared to BCL11B WT DN2a and DN3 thymocytes, respectively (Extended Data Fig. 8b). These changes had little correlation to mRNA levels[48] at the respective differentially accessible T_{EFF} loci (Extended Data Fig. 8c,d). The combined DN2a and DN3 (hereafter DN2a-DN3) ATAC-seq datasets identified 8,576 T_{EFF} loci (e.g. *Il2*, *Ifng*) that required both BCL11B and SMARCA4 for chromatin accessibility at these developmental stages (Fig. 4c,d). We also identified 4,463 SMARCA4-induced T_{EFF} loci at which the chromatin accessibility was greater in BCL11B cKO compared to BCL11B WT DN2a-DN3 thymocytes (e.g. *Il17a*, *Fcer1g*) (Fig. 4c,d and Extended Data Fig. 8e). The amplitude of chromatin accessibility at these BCL11B-repressed loci was substantially lower compared to BCL11B-induced loci in BCL11B WT DN2a-DN3 thymocytes (Extended Data Fig. 8f), suggesting that these loci were dampened at these stages of thymocyte differentiation. Considering the prominent role of BCL11B in alternative lineage exclusion[44, 45, 46], we used published ATAC-seq datasets[8] and found a greater overlap between BCL11B-repressed compared to BCL11B-induced T_{EFF} loci and the accessibility landscapes of natural killer (NK) and innate lymphoid cells (ILCs) ILC1 and ILC3, but not ILC2 (Fig. 4e and Extended Data Fig. 8g), consistent with the essential role of BCL11B in ILC2 identity and function[49]. Taken together, these results suggested that BCL11B worked cooperatively with SMARCA4 to maintain a poised accessibility state at many T_{EFF} loci in DN2a-DN3 thymocytes, while dampening loci shared with alternative lineage programs.

BCL11B maintains mSWI/SNF occupancy at T_{EFF} loci

BCL11B was reported as a tightly associated, dedicated (i.e. doesn't associate with other complexes or exist in nucleoplasm as unassociated factor) T cell-specific subunit of the mSWI/SNF complex in a T acute lymphoblastic leukemia cell line (CCRF-CEM)[47]. To determine whether this interaction was observed in untransformed primary thymocytes, we conducted reciprocal co-immunoprecipitation (co-IP) studies in nuclear lysates from total thymocytes isolated from wild-type mice at an IP efficiency that depleted the target antigen from the lysate flow-through. We found little to no detectable interaction between BCL11B and SMARCA4 or PBRM1, a core subunit of the Polybromo mSWI/SNF complex[43], in salt stringency ranging 50-300 mM for IP or wash conditions (Fig. 5a), while a physical interaction between SMARCA4 and PBRM1 was detected at 300 mM salt concentration (Fig. 5a). Co-IP experiments using nuclear lysates from CCRF-CEM T cells in the same range of salt concentrations also detected no interaction between BCL11B and SMARCA4 or PBRM1 (Extended Data Fig. 8h).

To test whether BCL11B and mSWI/SNF subunits were in discrete complexes, we determined the relative density of BCL11B-containing protein complexes. Contrary to previous studies[47], we found that BCL11B-associated complexes were significantly more dense than canonical mSWI/SNF complexes in both total thymocytes from wild-type mice (SMARCA4 fractions 10-15 vs. BCL11B fractions 15-22) and CCRF-CEM cells (SMARCA4 fractions 12-16 vs. BCL11B fractions 15-18) (Fig. 5b and Extended Data Fig. 8i). Treatment with benzonase endonuclease did not alter the density sedimentation of the respective complexes through the glycerol gradient (Extended Data Fig. 8j), indicating the readouts were not dependent on DNA or RNA in the nuclear lysates. These data indicated that BCL11B was not a tightly associated, dedicated mSWI/SNF subunit in T cell progenitors, and that it was largely associated in a distinct complex. However, we found that increasing the nuclear lysate concentration by an order of magnitude to drive protein interactions was sufficient to induce a weak but detectable physical interaction between BCL11B and SMARCA4 (Extended Data Fig. 8k), suggesting the possibility that BCL11B might exhibit weak, but meaningful affinity to mSWI/SNF complexes.

To investigate whether BCL11B facilitated the interaction between other transcription factors and mSWI/SNF to overcome the nucleosomal barriers at T_{EFF} loci, a process previously described as 'assisted loading' or 'competitive cooperativity'[50, 51], we performed BAF155 CUT&RUN in DN2-DN3 thymocytes sorted from BCL11B cKO or BCL11B WT mice. 78.9% of T_{EFF} loci whose chromatin accessibility depended on both SMARCA4 and BCL11B in DN2a-DN3 thymocytes exhibited a profound loss of BAF155 occupancy in BCL11B cKO compared to BCL11B WT DN2-DN3 thymocytes (Fig. 5c,d and Extended Data Fig. 8l), indicating that BCL11B was a critical determinant of mSWI/SNF recruitment at T_{EFF} loci. In contrast, 69.2% of BCL11B-repressed T_{EFF} loci that were also SMARCA4-induced (e.g. *Il17a*, *Tox2*) exhibited a modest gain of BAF155 occupancy in BCL11B cKO compared to BCL11B WT DN2-DN3 thymocytes (Fig. 5c,d and Extended Data Fig. 8l), indicating BCL11B inhibited mSWI/SNF recruitment to T_{EFF} loci enriched for NK and ILC function. mSWI/SNF occupancy at BCL11B-induced and BCL11B-repressed regions was highly correlated with the loss and gain of chromatin accessibility at the respective T_{EFF}

loci in BCL11B cKO DN2a-3 thymocytes (Fig. 5c,d), suggesting that BCL11B indirectly specified mSWI/SNF targeting to T_{EFF} loci at these developmental stages.

BCL11B and RUNX1 cooperate to maintain mSWI/SNF at T_{EFF} loci

Because BCL11B preferentially targets RUNX motifs[27] and RUNX1 was reported to physically interact with mSWI/SNF in a Jurkat T cell line[52], we investigated whether RUNX1 mediated the indirect cooperativity between BCL11B and mSWI/SNF. Published ChIP-seq datasets[27] indicated that BCL11B co-localized to the same SMARCA4-induced T_{EFF} loci as RUNX1 in DN2-DN3 thymocytes (Fig. 6a). Leveraging the ATAC-seq profiles from RUNX1 cKO and RUNX1 WT DN2a-DN3 thymocytes, we found that 81.1% of BCL11B-induced SMARCA4-induced T_{EFF} loci had decreased chromatin accessibility in RUNX1 cKO compared to RUNX1 WT DN2a-DN3 thymocytes (Fig. 6b). We also found that 84.3% of BCL11B-repressed SMARCA4-induced T_{EFF} loci exhibited loss in chromatin accessibility in RUNX1 cKO compared to RUNX1 WT DN2a-DN3 thymocytes (Fig. 6b), indicating that the increased accessibility observed at these regions in BCL11B cKO DN2a-DN3 thymocytes was dependent on RUNX1. These changes in chromatin accessibility had little correlation with local gene expression at the respective T_{EFF} loci (Extended Data Fig. 7b-g).

To test whether RUNX1 associated directly with mSWI/SNF in primary thymocytes, we performed reciprocal, depleting co-IPs from nuclear lysates of total thymocytes from wild-type mice. RUNX1 co-IPed with SMARCA4 at 300 mM salt concentrations independent of benzonase treatment (Fig. 6c). However, the majority of RUNX1 in the nuclear lysate did not interact with SMARCA4 and was observed in the IP flow-throughs (Fig. 6c), suggesting specific conditions, such as conformational states, might be necessary for interaction. To explore the potential heterogeneity of RUNX1 complexes, we performed density sedimentation in total thymocyte nuclear lysates from wild-type mice. RUNX1 was found across many fractions of varying densities (Fig. 6d), indicating distinct protein complexes competed for RUNX1 in the nucleus. Using the DN2-DN3 BAF155 CUT&RUN and RUNX1 ChIP-seq data from wild-type mice, we found that 56.6% of RUNX1-occupied genomic sites were also occupied by BAF155 (Extended Data Fig. 9a). Considering the strong preferential localization of mSWI/SNF to T_{EFF} loci compared to other accessible regions in the DN2-DN3 thymocyte genome, these results suggested that the fraction of RUNX1 that localized at T_{EFF} loci could be enriched in RUNX1-mSWI/SNF complexes relative to the heterogeneous pool of other RUNX1 complexes in the nucleus. We observed that most of the BCL11B in the nuclear lysate from total thymocytes from wild-type mice was pulled down by RUNX1 immunoprecipitation (Fig. 6c), suggesting that most BCL11B-associated complexes contained RUNX1. However, only a subset of the RUNX1 in the nucleus was pulled down by BCL11B immunoprecipitation (Fig. 6c), indicating the existence of heterogeneous RUNX1 complexes. Together, these data pointed to at least two distinct RUNX1 complexes, a BCL11B-associated complex and a mSWI/SNF-associated complex, that worked cooperatively to target and mediate remodeling of chromatin at T_{EFF} loci.

Next, we tested whether cooperativity between BCL11B and RUNX1 was required for their mutual targeting to SMARCA4-induced T_{EFF} loci. Analysis of published RUNX1 ChIP-seq data from Lin$^-$c-Kit$^+$CD25$^+$ *Bcl11b*$^{f/f}$Cre^{ERT2} DN2a-DN2b thymocytes[27] showed that 87.5% of BCL11B-induced SMARCA4-induced T_{EFF} loci exhibited loss in RUNX1 ChIP-seq read density in tamoxifen-treated (hereafter *Bcl11b*−/−) compared to ethanol-treated (hereafter *Bcl11b*+/+) *Bcl11b*$^{f/f}$Cre^{ERT2} DN2a-DN2b thymocytes (Fig. 6e,f and Extended Data Fig. 8m), indicating that RUNX1 localization at these SMARCA4-induced T_{EFF} loci was dependent on BCL11B. By contrast, 66.2% of BCL11B-repressed SMARCA4-induced T_{EFF} loci exhibited gain in RUNX1 ChIP-seq read density in *Bcl11b*−/−) compared to *Bcl11b*+/+ DN2a-DN2b thymocytes, albeit at a lower magnitude (Fig. 6e,f and Extended Data Fig. 8m), comparable to the gain in BAF155 occupancy at these same regions in BCL11B cKO compared to BCL11B WT DN2-DN3 thymocytes. Using the BAF155 CUT&RUN data from RUNX1 cKO and RUNX1 WT DN2-DN3 thymocytes, we found that 72.9% of BCL11B-repressed SMARCA4-induced T_{EFF} loci exhibited loss in BAF155 CUT&RUN fragment density in RUNX1 cKO compared to RUNX1 WT DN2-DN3 thymocytes (Fig. 6e,f). Together, these results suggested that BCL11B facilitated the prioritization of RUNX1-mSWI/SNF complexes away from more inflammatory T_{EFF} loci shared with NK and ILCs (e.g. *Il17a, Fcer1g*) and towards other T_{EFF} loci (e.g. *Il2, Ifng, Il27, Ctla4*), where a RUNX1-BCL11B associated complex and the RUNX1-mSWI/SNF complex potentially alternated occupancy at the same target sites in a ‘collaborative competition’[50, 51] that resulted in a net increase in binding of both complexes.

PU.1 partners with RUNX1 to poise T_{EFF} loci at ETP-DN2a stages

Next, we revisited the nature of the RUNX1-mediated induction of accessibility in ETP-DN2a thymocytes, prior to BCL11B expression. To identify potential transcription factors that cooperated with RUNX1 for mSWI/SNF recruitment to T_{EFF} loci in ETP and DN2a thymocytes, we performed differential transcription factor footprinting at all known transcription factor motifs that resided within T_{EFF} loci in ETP and DN2a thymocytes using the SMARCA4 cKO and SMARCA4 WT ATAC-seq datasets from these stages. Based on the differential footprint depth at target motifs between the SMARCA4 WT and SMARCA4-KO Tn5 insert profiles, PU.1 was identified as a potential RUNX1 partner for recruitment of mSWI/SNF to T_{EFF} loci in ETP-DN2a thymocytes (Fig. 7a,b), consistent with the reported PU.1-dependent RUNX1 genomic targeting[53] in ETPs and mSWI/SNF-dependent PU.1 genomic localization in myeloid cells[54, 55]. Analysis of published ChIP-seq datasets[39] indicated that PU.1 had strong preferential binding to SMARCA4-induced compared to SMARCA4-independent T_{EFF} loci in ETP and DN2a thymocytes (Fig. 7c), the same sites targeted by RUNX1 and mSWI/SNF complexes. Moreover, 88.1% of the SMARCA4-induced T_{EFF} loci occupied by PU.1 in ETP and DN2a thymocytes were occupied by BCL11B in DN2-DN3 thymocytes (Fig. 7d,e) when PU.1 is no longer expressed. These observations suggested that BCL11B maintained chromatin accessibility at T_{EFF} loci in DN2-DN3 thymocytes by maintaining the occupancy of RUNX1 and the associated mSWI/SNF complex that was initiated by PU.1 in ETPs.

To determine the functional importance of PU.1 in establishing chromatin accessibility at T_{EFF} loci, we compared accessibility landscapes generated from published ATAC-seq

datasets[53] between DN2a thymocytes from *Rosa*^{Cas9} mice transduced at the ETP stage with retrovirus encoding scrambled sgRNA (hereafter PU.1 WT) or sgRNA targeting *Spi1*, which encodes PU.1 (PU.1 KO). 63.3% of all SMARCA4-induced T_{EFF} loci and 63.4% of the BCL11B-induced subset were diminished in PU.1 KO compared to PU.1 WT DN2a thymocytes (Fig. 7f-h), with no correlation to local mRNA expression[53] at the respective T_{EFF} loci (Extended Data Fig. 10a,b). These observations indicated that PU.1 and BCL11B acted as stage-specific RUNX1 partners that allowed the cooperative recruitment of mSWI/SNF to T_{EFF} loci in ETP, DN2 and DN3 thymocytes (Extended Data Fig. 10c).

DISCUSSION

Here, we provide evidence that T cells specified lineage-specific effector activity through priming the chromatin landscape early in development, independently of the antigen receptor. This ‘effector licensing’ was mediated by a relay of transcription factors that conditions the genome for later targeting by signal-dependent transcription factors.

We identified that chromatin accessibility at T_{EFF} loci was induced in ETPs, before commitment to the T cell lineage in DN2b thymocytes, indicating distinct mechanisms underlying T effector poising and lineage commitment. However, we found considerable overlap in the molecular determinants, especially pertaining to the cooperativity between RUNX1 and PU.1 or RUNX1 and BCL11B[48, 53, 56]. RUNX1 was shown to be largely localized to accessible regions of the genome (82.5%); however, chromatin accessibility did not strictly correlate with some of the changes in RUNX1 occupancy between ETPs and the DN2b/DN3 stage, which are associated with lineage commitment[56]. These results are consistent with our finding that the majority of mSWI/SNF targeting to T_{EFF} loci in early T progenitors depended on RUNX1, but only a subset of RUNX1 in the nucleus physically associated with mSWI/SNF. Stoichiometric levels of RUNX1 were also shown to be limiting, as overexpression of RUNX1 resulted in localization at previously inaccessible regions enriched for NK or ILC-specific loci[56]. These results are consistent with our findings that *Bcl11b* deletion lead to a shift in RUNX1 and mSWI/SNF occupancy to T_{EFF} loci that are normally repressed by BCL11B and have significant overlap with the NK and ILC regulatory landscapes.

Our findings highlight the uncoupling of the developmental acquisition of specialized effector potential and the signal-triggered gene expression that ultimately elicits specific effector activity. These results could reflect a design principle that allows distinct lineages of the immune system to use the same signaling pathways to execute disparate roles, which collectively orchestrate pathogen elimination, immune memory and tissue repair.

METHODS

Mice

Mice used in this study were housed in pathogen-free facilities at the University of Chicago or Stanford University. All mice were housed in positively pressurized individually ventilated cage racks and changed in biological safety cabinets. Cage supplies are sanitized using hot water (180°F). Bedding and shredded paper enrichment were autoclaved and

cages were provided with irradiated food. Reverse Osmosis water was provided by an automated watering system directly to each cage. Rodent housing rooms were maintained at a 12-hour light / 12-hour dark cycle. Temperature and humidity were within the Guide for the Care and Use of Laboratory Animals recommended ranges: 68-79°F and 30-70% humidity. All experiments and animal use procedures were conducted in compliance with the National Institutes of Health Guide for the Care and Use of Laboratory Animals and were approved by the Institutional Animal Care and Use Committee (IACUC) at the University of Chicago and Stanford University. B6N.129S6-*Gt(ROSA)26Sortm1(CAG-tdTomato*,-EGFP*)Ees*/J (i.e. *Rosa26*^{nTnG}), B6.129-*Gt(ROSA)26Sortm1(cre/ERT2)Tyj*/J (i.e. *Rosa26*^{CreERT2}), B6.Cg-Tg(VAV1-cre)1Graf/MdfJ (i.e. *Vav1-iCre*) *and* C57BL/6J mice were purchased from Jackson Laboratories. *Smarca4*$^{f/f}$ mice were originally obtained from P. Chambon (University of Strasbourg)[57], *Bcl11b*$^{f/f}$ mice were provided by M. Leid (Oregon State University)[58] and *Runx1*$^{f/f}$ mice were provided by P. Liu (NIH/NHGRI), originally generated by D. Littman (New York University)[59]. These mice were bred to generate SMARCA4-KO (*Smarca4*$^{f/f}$*Rosa26*$^{CreERT2/nTnG}$), BCL11B cKO (*Vav1-Cre*$^{+}$ *Bcl11b*$^{f/f}$) and RUNX1-KO (*Runx1*$^{f/f}$*Rosa26*$^{CreERT2/nTnG}$) strains for experiments. Bone marrow was harvested at 2-4 months of age. Primary thymocytes were harvested at 4-6 weeks of age. Sex-matched littermates were used for all genetic perturbations.

Cell lines and culture

OP9-DL4 cells were provided by their inventor, J. C. Zúñiga-Pflücker (University of Toronto). OP9-DL4 cells were cultured at 37°C and 5% CO_2 in OP9 culture medium (MEM Alpha (Gibco) with 20% FBS (R&D Systems), 1% Penicillin-Streptomycin (Gibco)). CCRF-CEM (CCL-119) cells (human female) were purchased from ATCC. CCRF-CEM cells were authenticated by ATCC via short tandem repeat (STR) profiling. CCRF-CEM cells were cultured at 37°C and 5% CO_2 in RPMI (Gibco) containing with 10% FBS (R&D Systems), 2mM L-glutamine (Gibco), 10mM HEPES (Gibco), 1mM sodium pyruvate (Gibco), 1% Penicillin-Streptomycin (Gibco). All cell lines showed expected cell surface protein expression and pro-T cell development proceeded as expected.

Flow cytometry and cell sorting

Cells were incubated for 15 minutes at 4°C with relevant antibody mix diluted in T cell FACS buffer (2% FCS, 0.5% BSA, 10 mM EDTA in PBS). Flow cytometry data were acquired and cell sorting was performed using FACS Symphony S6, FACSAria Fusion, or FACSAria II equipped with a 70 μm nozzle (BD Biosciences). Fluorochrome-conjugated monoclonal antibodies specific for mouse CD4 (clone GK1.5 1:150), CD8a (clone 53-6.7 1:150), γδTCR (clone GL3 1:150), CD11b (clone M1/70 1:150), CD11c (clone N418 1:150), CD19 (clone 6D5 1:150), CD45R / B220 (clone RA3-6B2 1:150), NK-1.1 (clone PK136 1:150), Ly-6G/Ly-6C / Gr-1 (clone RB6-8C5 1:150), Erythroid Cells (clone TER-119 1:150), CD25 (clone PC61, 1:100), CD44 (clone IM7 1:100), CD45 (clone 30-F11 1:100), CD117 / c-Kit (clone 2B8 1:100), Ly-6A/E / Sca-1 (clone D7 1:100), CD69 (clone H1.2F3 1:100), CD62L (clone MEL-14 1:100), TCR-β (clone H57-597 1:100) were purchased from BioLegend. Dead cells were excluded using DAPI (Invitrogen 1:20).

Isolation of Lin^{-}Sca-1 c-Kit^{+} hematopoietic progenitors

Femurs and tibia of 2-4 month-old mice were mechanically liberated using a mortar and pestle to isolate bone marrow in OP9 media. Cells were filtered through 40 μm mesh strainer, red blood cells were lysed (BD PharmLyse) and CD4^{-} CD8^{-} CD11b^{-} CD11c^{-} CD19^{-} GR-1^{-} Ter119^{-} NK1.1^{-} γδTCR^{-} cells were enriched using Direct Lineage Cell Depletion Cocktail (Miltenyi Biotec). Cells were stained with fluorescent antibodies in T cell FACS Buffer (2% FCS, 0.5% BSA, 10 mM EDTA in PBS) and sorted for DAPI^{-} CD4^{-} CD8^{-} CD11b^{-} CD11c^{-} CD19^{-} B220^{-} GR-1^{-} Ter119^{-} NK1.1^{-} γδTCR^{-} Sca-1^{+} c-Kit^{hi} population into OP9 medium using aseptic FACS with Symphony S6, FACSAria Fusion, or FACS Aria II (BD Biosciences).

OP9 co-culture and differentiation

FACS-sorted primary Lin^{-} Sca-1^{+} c-Kit^{hi} progenitors were co-cultured with OP9-DL4 cells as previously described.[60] Briefly, sorted Lin^{-} Sca-1^{+} c-Kit^{hi} progenitors were resuspended in OP9 culture medium supplemented with 5 ng /mL Flt-3L (R&D Systems), 1 ng/mL IL-7 (PeproTech) and 2.5 μg/mL Plasmocin Prophylactic (InvivoGen), then seeded onto 80%-90% confluent OP9-DL4 plates. Progenitors were split onto fresh OP9-DL4 plates every 4 days via mechanical liberation (without trypsin). For tamoxifen-inducible deletion at day 4 of co-culture, (Z)-4-Hydroxytamoxifen (Sigma) dissolved in ethanol was added to the supplemented OP9 culture medium at 1 μM for 30 hours. An equivalent volume of ethanol was added to the control samples. After 30 hours, progenitor cells were replated onto fresh OP9-DL4 plates. On Day 8 of co-culture, progenitor cells were mechanically liberated from co-culture dishes and differentiating T cell subsets were isolated via FACS. Live (DAPI^{-}), lineage-negative (CD11b^{-} CD11c^{-} CD19^{-} B220^{-} GR-1^{-} Ter119^{-} NK1.1^{-} γδTCR^{-} EpCAM^{-}), DN (CD4^{-} CD8^{-}) gated cells were sorted as “ETP” (CD25^{-} c-Kit^{hi}), “DN2a” (CD25^{+} c-Kit^{hi}) and “DN3” (CD25^{+} c-Kit^{-}). For genetic perturbations, DN subsets were additionally gated for tdTomato or GFP based on Cre activity as reported by the *Rosa26*^{nTnG} allele. For inhibition of calcineurin activity, FK506 (Selleckchem) was added to supplemented OP9 culture medium at 30 nM at day 4 of co-culture. An equivalent volume of DMSO was added to the control samples. On Day 8 of co-culture, progenitors were mechanically liberated and FACS-sorted as described above.

Isolation of primary thymocytes

Thymi from 3-6 week-old mice were removed and small cortical incisions made prior to mechanical agitation with wide-bore glass pipettes in DMEM/F-12 (Gibco) to liberate thymocytes. BCL11B cKO thymi were digested with 1.25 μg/mL Collagenase IV (Sigma) and 1.0 μg/mL DNase I (Sigma) in DMEM/F-12 for 5 min at 37°C for efficient liberation of thymocytes. Cells were stained with antibodies in T cell FACS buffer and live, lineage-negative (DAPI^{-} CD11b^{-} CD11c^{-} CD19^{-} B220^{-} Gr-1^{-} Ter119^{-} NK1.1^{-} γδTCR^{-}) gated cells were sorted as “DP” (CD4^{+} CD8^{+} TCR-β^{lo} CD69^{-}), “CD4SP” (CD4^{+} CD8^{-} TCR-β^{hi}) and “CD8SP” (CD4^{-} CD8^{+} TCR-β^{hi}). For isolation of DN thymocytes, cells were initially enriched via negative selection against CD8a using MACS with CD8a (Ly-2) microbeads (Miltenyi Biotec). Live, lineage-negative (DAPI^{-} CD11b^{-} CD11c^{-} CD19^{-} B220^{-} Gr-1^{-}

Ter119$^-$ NK1.1$^-$ γδTCR$^-$) DN (CD4$^-$ CD8$^-$) cells were sorted as “ETP” (CD25$^-$ c-Kit^{hi}), “DN2a” (CD25$^+$ c-Kit^{hi}), “DN3” (CD25$^+$ c-Kit$^-$) and “DN4” (CD25$^-$ c-Kit$^-$ CD44$^-$).

Peripheral T cell isolation and stimulation

Spleen and lymph nodes from 3-6 week-old mice were isolated in RPMI 1640 (Gibco) supplemented with 10% FCS and 1% Penicillin-Streptomycin (10% RPMI). Cells were liberated by mincing with syringe plunger and filtered through 40 μm strainer. After ACK lysis, cells were stained with antibodies in T cell FACS buffer. Live, lineage-negative (DAPI$^-$ CD11b$^-$ CD11c$^-$ CD19$^-$ CB220$^-$ Gr-1$^-$ Ter119$^-$ NK1.1$^-$ γδTCR$^-$) T cells (TCR-β^{hi}) were sorted as “CD8$^+$ T_N” (CD8$^+$ CD4$^-$ CD44^{lo} CD62L^{hi}) and “CD4$^+$ T_N” (CD8$^-$ CD4$^+$ CD44^{lo} CD62L^{hi}). For *in vitro* T cell activation, 96-well tissue-culture-treated microtiter plates (Corning) were coated with 1 ug/ml anti-CD3ε (clone 145-2C11) and 2 ug/ml anti-CD28 (clone 37.51) and incubated at 37°C for 90 min. After 3 cold PBS washes, 200k FACS-sorted CD8$^+$ or CD4$^+$ T_N cells were added to each well in 10% RPMI and incubated for 72 h at 37°C, 5% CO_2. Live (DAPI$^-$), activated T cells were FACS sorted as “CD4$^+$ T_{EFF} *in vitro*” or “CD8$^+$ T_{EFF} *in vitro*”.

ATAC-seq sample preparation

ATAC-seq was performed as previously described[61] with minor modifications. For nuclei isolation of primary thymocytes or DN cells from OP9-DL4 co-cultures, 50,000-60,000 FACS-sorted cells were lysed in Thymocyte Hypotonic Buffer (25 mM HEPES, 5 mM $MgCl_2$, 0.05 mM EDTA, 10% Glycerol, 0.1% NP40). For nuclei isolation of peripheral naïve T cells or *in vitro* activated T cells, 50,000-60,000 FACS-sorted cells were lysed in ATAC lysis buffer (10 mM Tris pH 7.4, 10 mM NaCl, 3 mM $MgCl_2$, 0.1% Tween-20). Tagmentation reactions were performed for 30 minutes at 37°C using reagents from Illumina Tagment DNA TDE1 Enzyme and Buffer Kit. Tagmented DNA samples were purified with DNA Clean & Concentrator-5 kit (Zymo Research). Libraries were quantified by qPCR, amplified accordingly and purified using DNA Clean & Concentrator kit. Paired-end, dual-index sequencing was performed on the Illumina NextSeq500 platform.

RNA-seq sample preparation

50,000-100,000 primary thymocytes or DN cells from OP9-DL4 co-cultures were FACS-sorted directly into RULT lysis buffer from Qiagen RNeasy UCP Micro Kit and total RNA was extracted using manufacturer’s instructions. mRNA was enriched and RNA-seq libraries were constructed using the Illumina TruSeq Stranded mRNA Kit. Paired-end, dual-index sequencing was performed on the Illumina NovaSeq 6000 platform.

CUT&RUN sample preparation

CUT&RUN was performed as previously described[41] with minor modifications. Briefly, 500k cells were washed 3x in Wash Buffer (20 mM HEPES pH 7.5, 150 mM NaCl, 0.5 mM spermidine, 1x EDTA-free protease inhibitor cocktail (Roche)), then bound to Concanavalin-A beads (Bangs Laboratories) according to manufacturer’s instructions. Cells were incubated with 1:100 dilution of anti-BAF155 antibody (G. Crabtree) for 2h or overnight at 4°C in Permeabilization Buffer (1x Permeabilization Buffer (eBioscience), 0.5

mM spermidine, 1x EDTA-free protease inhibitor cocktail, 2 mM EDTA). Sample was then incubated with 700 ng/mL pA-MNase (S. Henikoff) in Permeabilization Buffer at 4°C for 1h. Digestion was performed in 0.5x Permeabilization Buffer supplemented with 2 mM $CaCl_2$ at 4°C for 1h. The reaction was stopped by the addition of 2x Stop Buffer (final concentration 100 mM NaCl, 10 mM EDTA, 2 mM EGTA, 20μg/mL glycogen, 25μg/mL RNase A (Thermo Fisher)) and the sample was incubated at 37°C for 20 min. Proteins in sample was then digested in 0.1% SDS and 250 μg/mL Proteinase K (New England Biolabs) for 2h at 56°C, shaking gently. CUT&RUN fragments were purified by phenol chloroform extraction. CUT&RUN libraries were generated using NEBNext UltraII DNA Library Prep Kit for Illumina coupled with NEBNext Multiplex Oligos for Illumina (New England Biolabs) with modifications optimized for small fragments as detailed in https://dx.doi.org/10.17504/protocols.io.wvgfe3w. Paired-end, dual-index sequencing was performed on the Illumina NextSeq500 platform.

Preparation of nuclear extracts

CCRF-CEM cells or thymocytes from 3-6 week-old mice were liberated as above and resuspended in Thymocyte Hypotonic Buffer supplemented with 1 mM DTT, 1 mM PMSF and 1x cOmplete protease inhibitor cocktail (Roche). Following 15-minute hypotonic lysis on ice, nuclei were centrifuged at 700 x g and resuspended in 600uL per 200e6 cells of Buffer C (10 mM HEPES pH 7.5, 100 mM NaCl, 0.1 mM EDTA, 3 mM $MgCl_2$, 10% Glycerol). Ammonium sulfate was added drop-wise to 150 mM and samples rotated at 4°C for 30 minutes. Lysates were centrifuged at 435,400 x g (100,000 RPM) in TLA 120.2 rotor (Beckman Coulter) for 10 minutes at 4°C. Supernatant was transferred to an ice-chilled tube and proteins were precipitated with 0.33 mg/μL ammonium sulfate on ice for 20 minutes. Lysates were centrifuged once more at 435,400 x g for 10 minutes. Supernatant was discarded and pellets were used for downstream applications.

Density gradient sedimentation

Nuclear extracts were reconstituted in 0% glycerol HEMG buffer (25 mM HEPES pH 7.9, 0.1 mM EDTA, 12.5 mM $MgCl_2$, 100 mM NaCl) supplemented with 1 mM DTT, 1 mM PMSF and 1x cOmplete protease inhibitor cocktail. For samples treated with benzonase, benzonase (Sigma 9025-65-4) was added to the nuclear extract (≥25 units/μL) and sample was pipette-mixed and incubated on ice for 30 minutes. 1 mg of nuclear extract (200 μL) was overlaid onto a 10-30% glycerol gradient (in HEMG buffer) prepared in 14 x 89 mm polypropylene centrifuge tubes (Beckman Coulter). Tubes were centrifuged at 274,400 x g (40,000 RPM), 16 hours, 4°C in a SW41-Ti rotor. 500 μL fractions were collected and subjected to immunoblotting directly or after concentrating using 50 μL StrataClean Resin (Agilent Technologies).

Co-immunoprecipitation

Nuclear extracts were reconstituted in EB300, EB150, or EB50 buffer (50 mM Tris-HCl pH 7.5, 1 mM EDTA, 1 mM $MgCl_2$, 1% NP-40, with 300 mM or 150 mM or 50 mM NaCl, respectively), supplemented with 1 mM DTT, 1 mM PMSF and 1x cOmplete protease inhibitor cocktail tablet and volume adjusted to 1 mg/mL or 10 mg/mL. Nuclear extracts were incubated overnight with antibodies against SMARCA4 (Abcam, clone EPNCIR111A,

0.01 ug/ul), PBRM1/BAF180 (Cell Signaling Technology, clone D3F7O, 1:50), BCL11B (Cell Signaling Technology, clone D6F1, 1:100), RUNX1 (Thermo, polyclonal; Cell Signaling Technology, clone D4A6, 0.01 ug/ul), mouse IgG (Santa Cruz, 0.01 ug/ul) or rabbit IgG (EMD Millipore, 0.01 ug/ul). Washed Protein G Dynabeads (Invitrogen) were added to samples for 3 hours. Immunoprecipitants (IPs) were harvested by magnetic separation and remaining 'supernatant' was stored as "flow-thru" samples. IP samples were washed 3 times in EB300, resuspended in LDS loading buffer with 100 mM DTT and incubated at 70°C for 10 minutes. Dynabeads were removed and remaining samples were subjected to Western blots.

Immunoblotting

Proteins were separated on a 4-12% PAGE gel (Invitrogen), transferred onto a PVDF membrane (Millipore), blocked with 5% milk in TBST (20 mM Tris pH 7.6, 150 mM NaCl, 0.1% Tween-20) for 1 hour at RT and incubated overnight at 4°C with primary antibodies: rabbit anti-mouse BAF155 (courtesy of Crabtree Laboratory, 1:1000), rabbit anti-SMARCA4 (Abcam, clone EPNCIR111A, 1:1000), mouse anti-human SMARCA4 (Santa Cruz Biotechnology, clone G-7, 1:1000), rabbit anti-PBRM1 (Cell Signaling Technology, clone D3F7O, 1:1000), rabbit anti-human BCL11B (Thermo, polyclonal, 1:1000), mouse anti-human RUNX1 (Santa Cruz Biotechnology, clone A-2, 1:1000). Membranes were washed three times with TBST and incubated with secondary fluorophore-conjugated antibodies (Bio-Rad) for 1 hour at RT. Membranes were washed three times with TBST and imaged using Bio-Rad ChemiDoc MP Imaging System.

ATAC-seq pre-processing and peak definitions

Adaptor sequences were trimmed using *SeqPurge* (v2019_11). Trimmed reads were mapped to mm10 mouse genome assembly using *Bowtie2* (v2.2.9) with settings *--very-sensitive -X 2000*. PCR duplicates were removed using *Picard* (v2.21.8) *MarkDuplicates REMOVE_DUPLICATES=true VALIDATION_STRINGENCY=LENIENT*. Reads with MAPQ scores below 30 were purged using *samtools* (v1.9) *view* with settings *-b -q 30 -f 2 -F 1804*. Peaks were called for each sample using *MACS2* (v2.2.7.1) with settings *--shift -75 --extsize 150 --nomodel --call-summits --nolambda --keep-dup all -p 0.01 --min-length 100*. For each sample, a 501 bp fixed-width peak set was generated by extending the MACS2 summits by 250 bp in both directions. Peaks were ranked by significance (MACS2 peak score) and overlapping peaks with lower peak scores were removed iteratively to create non-overlapping sample peak sets. To facilitate comparison of peaks across samples, each peak's 'score-per-million' (SPM) was calculated by dividing the peak score by the sum of all peak scores in the sample, divided by 1 million. All sample peak sets were merged, less significant overlapping peaks removed and remaining peaks were filtered for those that were observed in at least two samples with an SPM value ≥ 5. We removed peaks mapping to chrY as well as any that spanned genomic regions containing "N" nucleotides. We then removed any peak that overlapped with those called in activated B cell samples to create a "Total T cell" merged peak set. To identify T effector-specific peaks, sample peak sets from only peripheral T effector samples were merged and processed as above for non-overlapping, robust, reproducible peaks purged of activated B cell peaks. To account for less robust but significant T effector peaks which were robustly accessible in early thymocyte

development, we added filtered sample peaks from ETP-DN4 stages (reproducible, SPM ≥ 5) that overlapped with reproducible T effector peaks at SPM ≥ 2 to this initial filtered T effector merged set. This merged set was again filtered for non-overlapping, robust (SPM ≥ 5), reproducible peaks purged of activated B cell peaks to generate the final union peak set referred to as 'T effector loci' (T_{EFF} loci). Peaks from the "Total T cell" merged peak set that did not overlap with T_{EFF} loci are collectively referred to as 'Non-T_{EFF} peaks'. To generate peak-by-sample count matrices, ATAC-seq fragment counts within each peak were normalized by the number of inserts intersecting nucleosome-depleted promoter regions (−300 bp to +100 bp relative to transcriptional start-sites).

Differential chromatin accessibility analysis

Differential accessibility was assessed using *Limma* (v3.50.1) in R. P-values for regression coefficient estimates representing variation due to genotype were corrected for multiple-testing using the Benjamini-Hochberg false discovery rate (FDR) method. Peaks exhibiting FDR < 0.1 were regarded as significant. To define a collective set of 'SMARCA4-dependent T_{EFF} loci', we pooled the peaks that become differentially accessible at the respective ETP (n=5,209), DN2a (n=6,985) and DN3 (n=3,393) stages for a grand total of 15,587 SMARCA4-induced peaks. To define a collective set of 'SMARCA4-independent T_{EFF} loci', we selected peaks with FDR > 0.5 and exhibiting differences in fold-change of normalized ATAC-seq fragments between SMARCA4 WT and SMARCA4 cKO samples at > 0.9 and < 1.1 at all stages of T cell development that were assessed (n=16,374 peaks). One-sided Fisher's exact tests were performed for over-representation in quadrants of fold-change vs. fold-change scatter plots. Mann-Whitney *U*-tests were performed to identify significant differences at medians of pairwise comparisons in cumulative distribution function plots.

Transcription factor motif enrichment and footprinting

Enrichment of transcription factor binding motifs within peaks was computed using *HOMER* (v4.11.1) *findMotifsGenome.pl* with settings *-size 501 -mask*. TF footprinting was assessed by plotting normalized counts of ATAC 5' inserts spanning a 200 bp window relative to the motif center. Footprint counts were normalized by the number of inserts intersecting nucleosome-depleted promoter regions (−300 bp to +100 bp relative to transcriptional start-sites). TF footprint depth was calculated by dividing the "flanking accessibility" by the "footprint base". Footprint base = normalized ATAC insert counts within +/− 5 bp of motif center. Flanking accessibility = normalized ATAC insert counts within 20 bp regions flanking the ends of the footprint base. Footprint base and flanking accessibility counts were divided by the "footprint background" which was the normalized ATAC insert counts at a 40 bp region 1 kb upstream of the motif center.

RNA-seq data processing

Adaptor sequences were trimmed using *SeqPurge* (v2019_11). Trimmed RNA-seq reads were mapped to the mm10 mouse genome assembly using *TopHat* (v2.1.1) with settings *–microexon-search*. Unmapped, unpaired and low quality reads (MAPQ < 5) were removed using *samtools* (v1.9) *view* with settings *-q 5 -f 2*. Paired reads were counted for each gene using *featureCounts* from *Subread* (v2.0.1). 'Transcripts-per-million' (TPM) values

were calculated for each gene to quantify the relative abundance of transcripts for clustering analysis. 'Trimmed mean of M values' (TMM) was calculated for each gene for differential comparisons across samples using *edgeR* (*calcNormFactors*). Common dispersions were estimated using *estimateCommonDisp* and Benjamini-Hochberg false discovery rates (FDRs) were calculated for pairwise comparisons using *exactTest*. Genes exhibiting FDR < 0.05 were regarded as significant.

Protein interaction network

Known subunits of the mSWI/SNF, ISWI, INO80, COMPASS, Cohesin complexes and the TFs representing the top motif enrichments of accessible T_{EFF} loci in early thymocyte progenitors were used as inputs to the *STRING* (v11.5) database (http://string-db.org/) to construct a putative protein-protein interaction network. Parameters were set to *Full STRING network* for *high confidence (0.700)* interactions using *Experiments*, *Databases* and *Textmining* as Active Interaction Sources. MCL clustering of the interaction network was performed with *inflation parameter = 2*.

CUT&RUN data processing

CUT&RUN reads were mapped to mm10 mouse genome assembly using *Bowtie2* (v2.2.9) with settings *--local --very-sensitive-local –no-unal –no-mixed –no-discordant –phred33 -I 10 -X 700*. PCR duplicates were removed using *Picard* (v2.21.8) *MarkDuplicates REMOVE_DUPLICATES=true VALIDATION_STRINGENCY=LENIENT*. Reads with MAPQ scores below 30 were purged and excluded from downstream analysis using *samtools* (v1.9) *view -b -q 30 -f 2 -F 1804*. To generate ATAC peak-by-sample count matrices, CUT&RUN fragment counts within each peak were normalized by the number of fragments intersecting nucleosome-depleted promoter regions (−300 bp to +100 bp relative to transcriptional start-sites).

ChIP-seq data processing

ChIP-seq reads were mapped to mm10 mouse genome assembly using *Bowtie2* (v2.2.9) with settings *--very-sensitive -X 2000*. PCR duplicates were removed using *Picard* (v2.21.8) *MarkDuplicates REMOVE_DUPLICATES=true VALIDATION_STRINGENCY=LENIENT*. Reads with MAPQ scores below 30 were purged and excluded from downstream analysis using *samtools* (v1.9) *view -b -q 30 -F 1796*. To generate ATAC peak-by-sample count matrices, ChIP-seq read counts within each peak were normalized by sequence depth.

Genome Browser and Heatmap Visualizations

BedGraph files for ATAC-seq, ChIP-seq and CUT&RUN datasets were generated using *bedtools* (v2.27.1) *genomecov* and normalized as described above. BedGraphs were converted to BigWig format using *bedGraphToBigWig* (v4) and uploaded to the UCSC genome browser (http://genome.ucsc.edu/) for visualization. Heatmaps of normalized fragments/reads across genomic regions of interest were visualized using *deepTools* (v3.5.1) *computeMatrix* and *plotHeatmap* with settings *-bs 100 --missingDataAsZero --skipZeros --referencePoint center*.

Statistics and reproducibility

All experimental findings were reliably reproduced with at least 2 biologically independent replicates for all experiments (except for ATAC-seq of CD4 SP and CD4 naive T cells for which data was only taken from one biological replicate as they largely recapitulate the data from CD8 SP and CD8 Naive T cells (performed with two biological replicates) and is not the stage in T development the manuscript focuses on). No statistical method was used to determine sample size. The number of replicates performed was determined based on those of previous related studies[42, 56, 62, 63, 64]. No animals or samples were excluded from analysis. No method of randomization was used. Investigators were not blinded to experimental group allocations. All controls and perturbations were performed on sex-matched littermates. All experimental and bioinformatic processing for control and perturbation groups was performed identically, together and in parallel for each replicate. All statistical tests performed were non-parametric. For all statistical tests, P-values, sample sizes and test “sidedness” (if applicable) are provided.

Extended Data

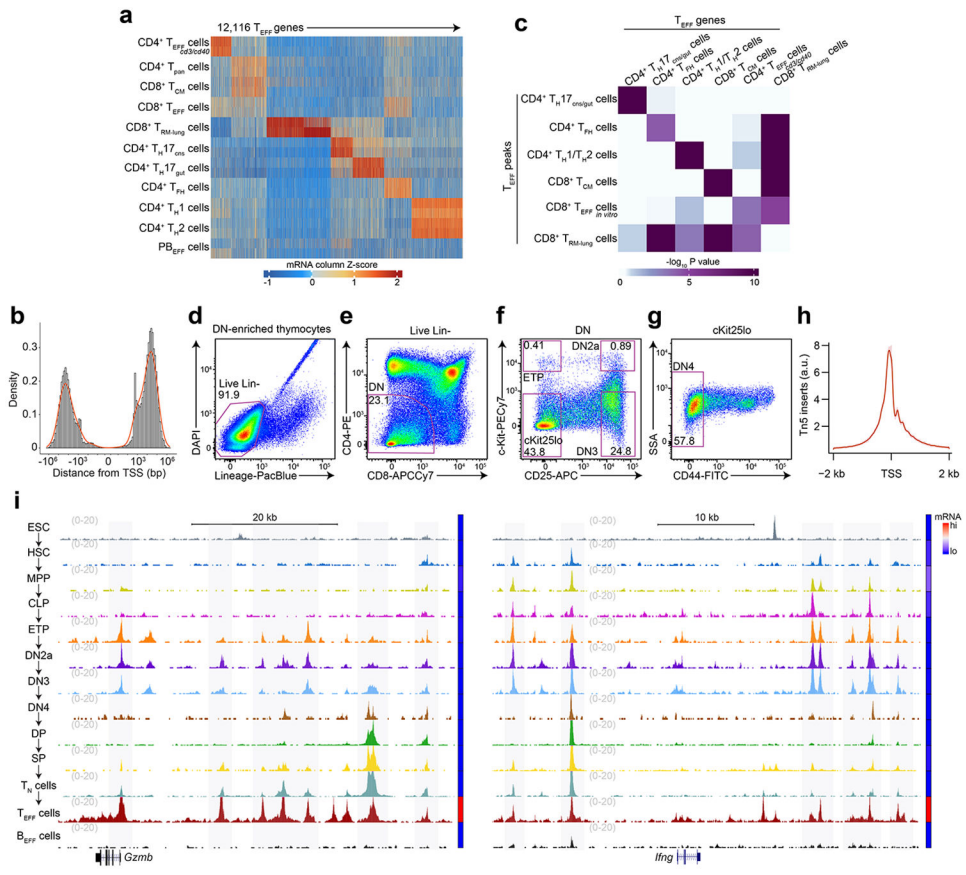

Extended Data Figure 1. T effector loci reflect the chromatin and transcriptional profiles of major T effector subtypes.

a, Heatmap of Z scores of TPM-normalized RNA-seq reads across the k-means clustered (k=7) transcriptomes (less genes robustly expressed in B_{EFF} cells) of sorted $CD4^{+}CD44^{+}TCR\beta^{lo}$ splenic T cells[21] 18h post-injection with CD3/CD40 Abs

(hereafter CD4$^+$ T_{EFF} *cd3/cd40*), splenic CD19$^-$CD8$^-$TCRβ$^+$CD4$^+$ T cells[21] (hereafter CD4$^+$ T_{pan}), T_{CM}, CD8$^+$ T_{EFF}, T_{RM}, T_H17_{CNS}, T_H17_{gut}, T_{FH}, T_H1, T_H2 and CD11b$^-$NK-1.1$^-$TCRβ$^-$CD138$^+$Blimp1^{int}MHCII^{hi} plasmablast cells[21] (hereafter PB_{EFF}) (n=2 each). **b,** Distribution of genomic displacement of T effector loci (hereafter T_{EFF} loci) in relation to the nearest TSS (signed logarithmic scale). **c,** Heatmap of statistical enrichment (one-sided Fisher's exact test) of T_{EFF} peaks whose nearest gene is in RNA-seq k-means cluster i (horizontal axis) within an ATAC-seq k-means cluster j (vertical axis; see Fig. 1a). **d-g,** Representative flow cytometry plots illustrating gating strategy for *in vivo* DN thymocyte FACS. **h,** Representative distribution (for all ATAC-seq samples) of normalized Tn5 insertions within 2 kb of transcriptional start-sites (TSS). **i,** Representative genome browser of ATAC-seq in ESC[29], HSC[11], MPP[11], CLP[11], ETP, DN2a, DN3, DN4, DP, CD8 SP, T_N, T_{EFF} cells and B_{EFF} cells at *Gzmb* (T_{EFF}=CD8$^+$ T_{EFF} *in vitro*) and *Ifng* (T_{EFF}=T_H1) loci (1 of n=2 for each). Adjoined bars indicate RNA-seq-determined transcripts-per-million (TPM) in each cell type.

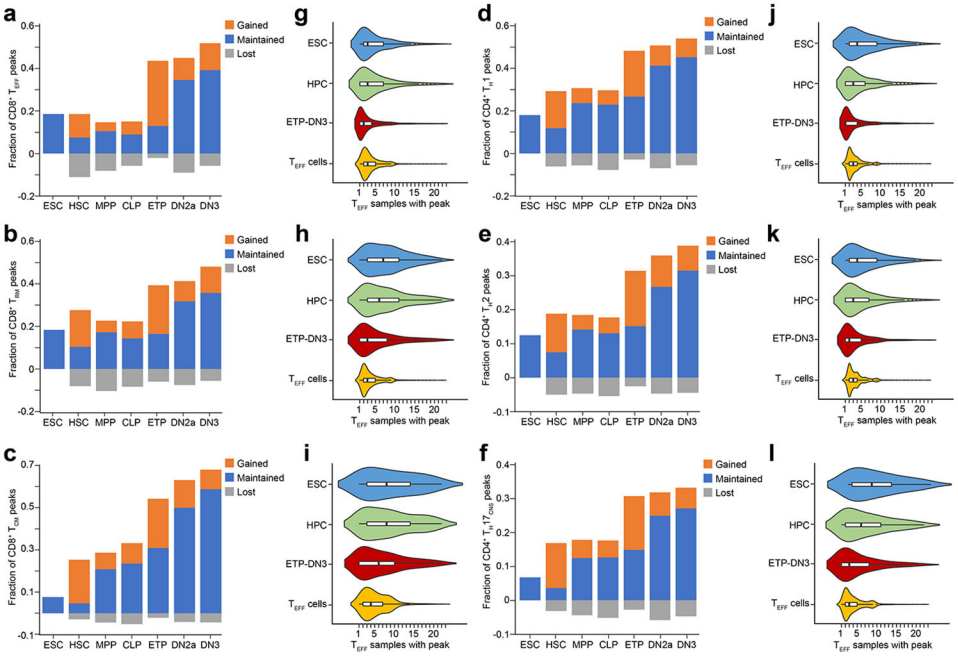

Extended Data Figure 2. Establishment and maintenance of chromatin accessibility at T_{EFF} loci in early T cell development.

a-f, Bar plots representing the fraction of CD8$^+$ T_{EFF}-specific (**a**), CD8$^+$ T_{RM}-specific (**b**), CD8$^+$ T_{CM}-specific (**c**), CD4$^+$ T_H1-specific (**d**), CD4$^+$ T_H2-specific (**e**), CD4$^+$ T_H17-specific (**f**) ATAC-seq peaks that became accessible (orange), are maintained accessible from previous stage (blue) or are no longer accessible relative to previous stage (gray) at ESC, HSC, MPP, CLP, ETP, DN2a and DN3 stages. **g-l,** Corresponding violin plots (boxes represent 25th, 50th and 75th percentiles; whiskers represent median +/− 1.5 interquartile range) representing the number of overlap between each ATAC-seq peak from CD8$^+$ T_{EFF}-specific (**g**), CD8$^+$ T_{RM}-specific (**h**), CD8$^+$ T_{CM}-specific (**i**), CD4$^+$ T_H1-specific (**j**), CD4$^+$ T_H2-specific (**k**), CD4$^+$ T_H17-specific (**l**) ATAC-seq profiles, grouped by the developmental

windows (ESC, HPC, ETP-DN3 and respective T_{EFF} cells) during which the ATAC-seq peak first became accessible.

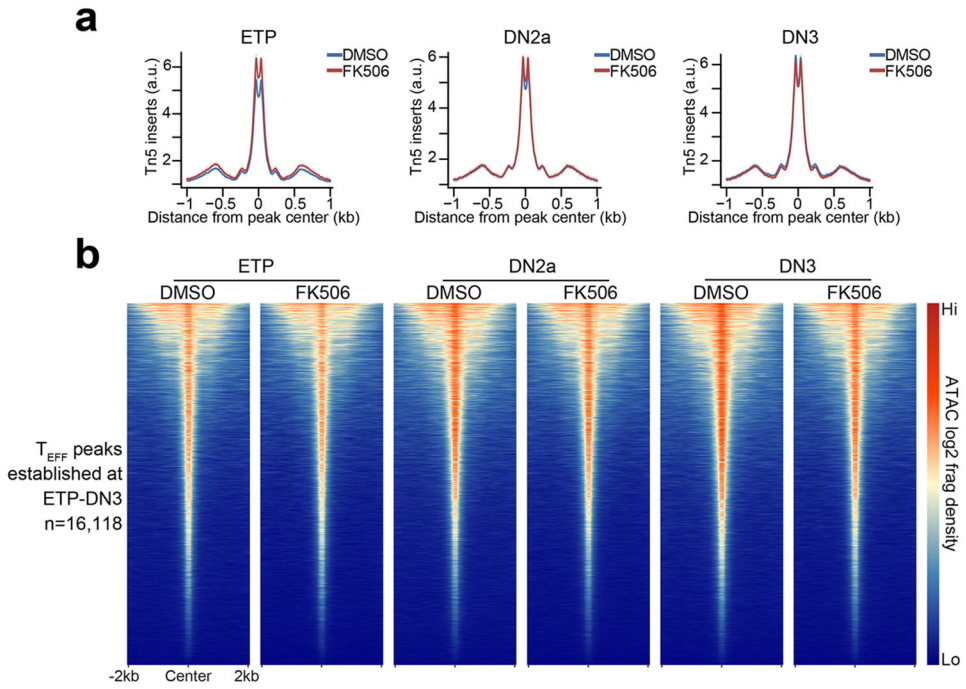

Extended Data Figure 3. Chromatin accessibility at T_{EFF} loci in early T cell progenitors is not dependent on calcineurin activity.

a, Representative aggregate histograms (1 of n=2) of ATAC-seq Tn5 insertions in *in* vitro differentiated FK506-treated (calcineurin inhibitor) vs. DMSO-treated (control) ETP-DN3 thymocytes at T_{EFF} loci that first became accessible in ETP-DN3 thymocytes. **b,** Representative heatmaps (1 of n=2) of ATAC-seq in *in* vitro differentiated FK506-treated (calcineurin inhibitor) vs. DMSO-treated (control) ETP-DN3 thymocytes at T_{EFF} loci that first become accessible in ETP-DN3 thymocytes.

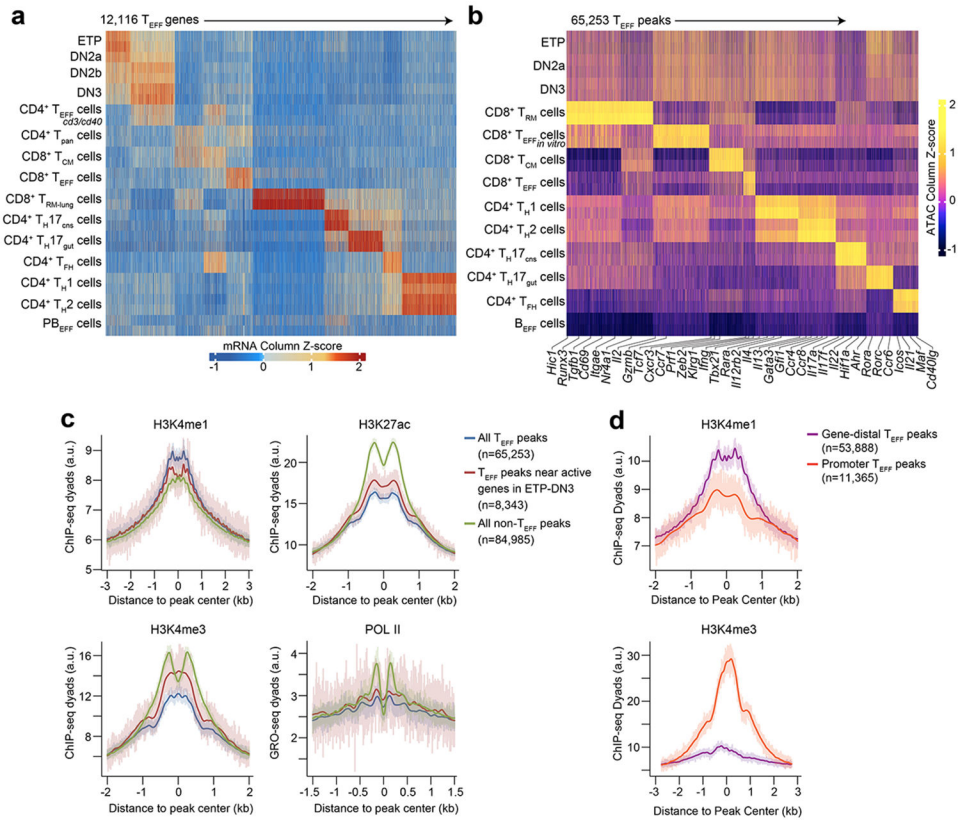

Extended Data Figure 4. Enhancer priming mediates early chromatin accessibility at T_{EFF} loci.

a, Heatmap of Z scores of TPM-normalized RNA-seq reads across the k-means clustered (k=10) transcriptomes (less genes robustly expressed in PB_{EFF} cells) of ETP, DN2a, $Lin^{-}c\text{-}Kit^{int}CD25^{hi}CD44^{hi}CD4^{-}CD8^{-}$ (DN2b), DN3, $CD4^{+}$ T_{EFF} *cd3/cd40*, $CD4^{+}$ T_{pan}, T_{CM}, $CD8^{+}$ T_{EFF}, T_{RM}, T_H17_{CNS}, T_H17_{gut}, T_{FH}, T_H1 and T_H2 cells (n=2 for each). **b,** Heatmap of Z scores of TSS-normalized ATAC-seq fragments across the k-means clustered (k=9) T_{EFF} loci in ETP, DN2, DN3, T_{RM}, $CD8^{+}$ T_{EFF} *in vitro*, $CD8^{+}$ T_{EFF}, T_{CM}, T_H1, T_H2, T_H17_{CNS}, T_H17_{gut}, T_{FH} cells and B_{EFF} cells (n=2 each). Labeled columns highlight ATAC-seq peaks whose nearest gene represents a canonical gene reflective of a distinct T effector program. **c,** Representative aggregate histograms of H3K4me1[31] (1 of n=2), H3K4me3[31] (1 of n=2), H3K27ac[32] (1 of n=2) or RNA Polymerase II[31] (POL II) (1 of n=2) ChIP-seq or GRO-seq dyads intersecting all T_{EFF} loci (blue), T_{EFF} loci near active genes in ETP-DN3 cells (blue) and all non-T_{EFF} loci (green) in DN2-DN3 thymocytes. **d,** Representative aggregate histograms of H3K4me1[31] (1 of n = 2), H3K4me3[31] (1 of n = 2) ChIP-seq dyads at promoter vs. gene-distal T_{EFF} loci in DN2-DN3 thymocytes.

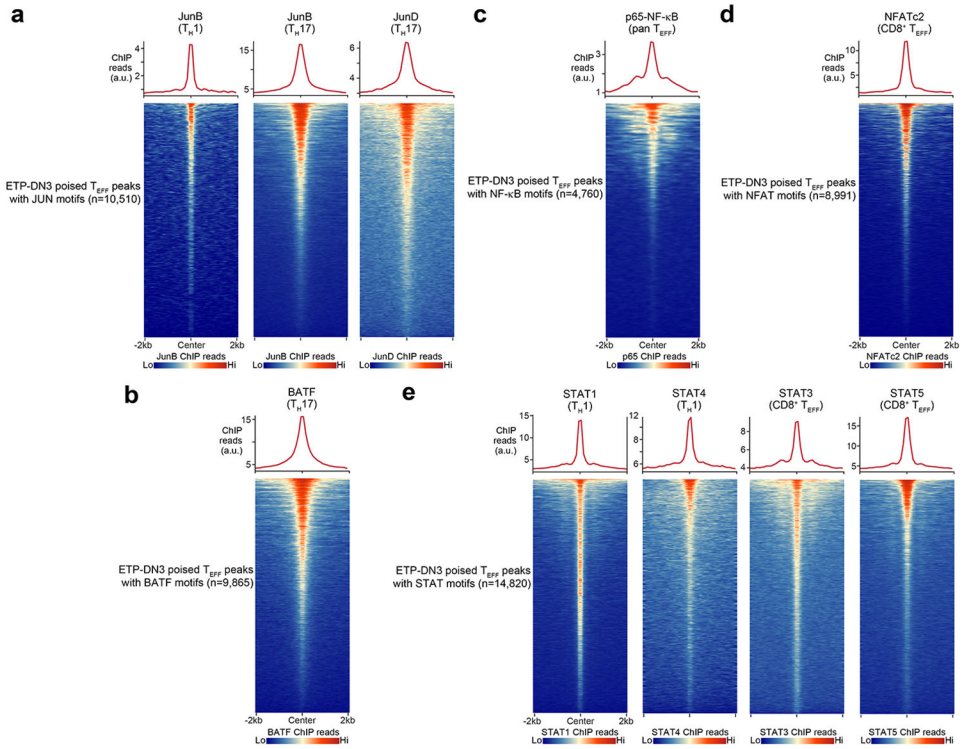

Extended Data Figure 5. Signal-regulated transcription factors localize to developmentally poised T_{EFF} loci in activated T_{EFF} cells.

a, Heatmaps and aggregate histograms of JUNB occupancy (ChIP-seq[45]) in T_H1 cells (n=1), JUNB in T_H17 cells[40] (1 of n=2), JUND occupancy (ChIP-seq[40]) in T_H17 cells (n=1) at T_{EFF} loci that contain Jun motifs. **b,** Heatmap and aggregate histogram of NFκB-p65 occupancy (ChIP-seq[43]) in *in vitro* activated T_{EFF} cells (1 of n=2) at T_{EFF} loci that contain NFκB-p65 motifs. **c,** Heatmap and aggregate histogram of NFATc2 occupancy (ChIP-seq[41]) in CD8+ T_{EFF} cells (n = 1) at T_{EFF} loci that contain NFATc2 motifs. **d,** Heatmap and aggregate histogram of BATF occupancy (ChIP-seq[39]) in T_H17 cells (1 of n=2) at T_{EFF} loci that contain BATF motifs. **e,** Heatmaps and aggregate histograms of STAT1 occupancy (ChIP-seq[6]) in T_H1 cells (n=1), STAT4 occupancy in T_H1 cells (ChIP-seq[44]) (1 of n=2), STAT3 occupancy (ChIP-seq[42]) in CD8+ T_{EFF} cells (1 of n=2) and STAT5 occupancy (ChIP-seq[42]) in $CD8^+$ T_{EFF} cells (1 of n=2) at T_{EFF} loci that contain STAT motifs. For this figure only, T_{EFF} loci (rows) in each heatmap were sorted independently and do not correspond to other heatmaps in the group.

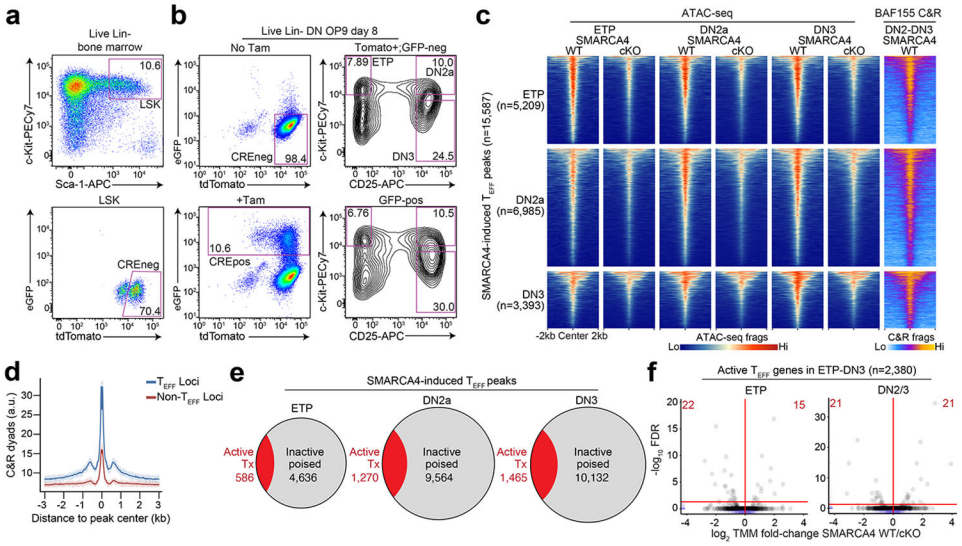

Extended Data Figure 6. *Smarca4* deletion inhibits chromatin poising of T_{EFF} loci in DN thymocytes.

a, Representative gating strategy for FACS of primary Lin$^-$ Sca-1$^+$ c-Kit$^+$ hematopoietic progenitors without Cre activity from *Smarca4*$^{f/f}$*Rosa*$^{CreERT2/nTnG}$ bone marrow cells. **b,** Representative gating strategy for FACS of ETP-DN3 thymocytes with or without Cre activity from OP9-DL4 *in vitro* differentiation co-cultures. **c,** Representative heatmaps of normalized ATAC-seq in *in vitro* differentiated SMARCA4 WT vs. SMARCA4 cKO ETP (1 of n=3), DN2a (1 of n=3) and DN3 (1 of n=2) thymocytes and BAF155 occupancy (CUT&RUN) in DN2-DN3 thymocytes (1 of n=3) across SMARCA4-induced T_{EFF} loci that first became accessible in ETP, DN2a and DN3 stages (rows). **d,** Representative aggregate histograms of BAF155 occupancy (CUT&RUN) in DN2-DN3 thymocytes (1 of n=3) across T_{EFF} loci (blue) and Non-T_{EFF} loci (red). **e,** Fraction of transcriptionally active SMARCA4-induced loci in ETP, DN2a, and DN3 thymocytes (n=2 each). **f,** Volcano plots of differential gene expression between *in vitro* differentiated SMARCA4 WT vs. SMARCA4 cKO ETP and DN2-DN3 thymocytes (n = 2 each) across actively transcribed T effector genes. Marginal rugs (blue lines) indicate distribution of values along each axis.

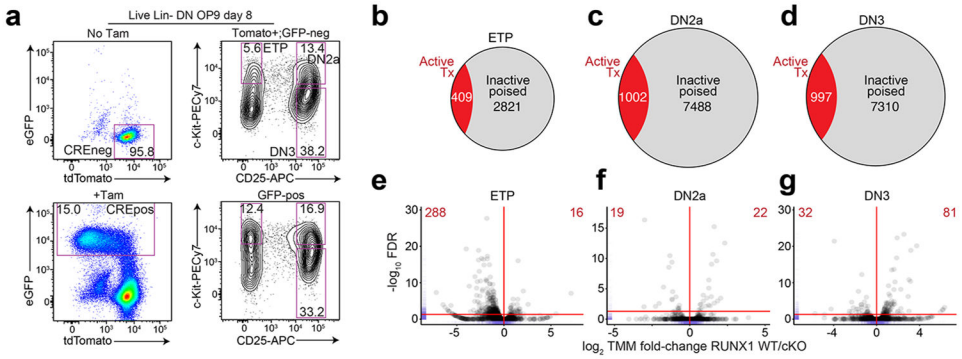

Extended Data Figure 7. *Runx1* perturbation in early T cell development.

a, Representative gating strategy for FACS of ETP-DN3 thymocytes with or without Cre activity from OP9-DL4 *in vitro* differentiation co-cultures derived from Lin$^-$Sca-1$^+$c-

Kit^{hi} hematopoietic progenitors of *Runx1*$^{f/f}$*Rosa*$^{CreERT2/nTnG}$ mice. **b-d,** Fraction of transcriptionally active RUNX1-induced loci in ETP (**b**), DN2a (**c**) and DN3 (**d**) thymocytes (n=2). **e-g,** Volcano plot of differential gene expression between *in vitro* differentiated RUNX1 WT vs. RUNX1 cKO ETP (**e**), DN2a (**f**) and DN3 (**g**) thymocytes (n=2) across actively transcribed T effector genes. Marginal rugs (blue lines) indicate distribution of values along each axis.

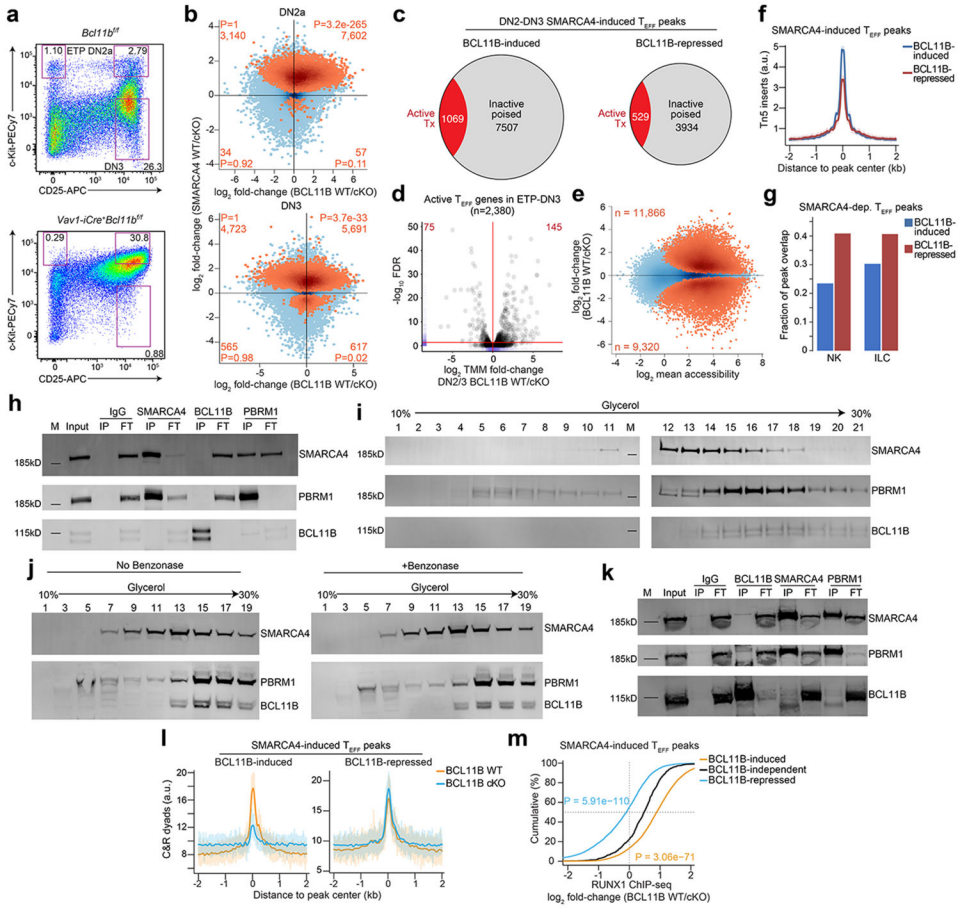

Extended Data Figure 8. SMARCA4 and BCL11B cooperate indirectly to promote chromatin accessibility at T effector loci in DN thymocytes.

a, Representative gating strategy for FACS of DN2-DN3 thymocytes from sex-matched littermates of *Vav1-iCre*$^{+}$ *Bcl11b*$^{f/f}$ or *Bcl11b*$^{f/f}$ mice. **b,** Top: Scatter plot depicting the $\log_2$ fold-change of normalized ATAC-seq fragments at T_{EFF} loci between sorted BCL11B WT vs. BCL11B cKO primary DN2a thymocytes (n=2; horizontal axis) and *in vitro* differentiated SMARCA4 WT vs. SMARCA4 cKO DN2a thymocytes (n=3; vertical axis). SMARCA4-induced T_{EFF} loci (Benjamini-Hochberg-corrected FDR < 0.1) peaks highlighted in orange. Number and statistical enrichment of SMARCA4-induced T effector loci (determined by one-sided Fisher's exact test) within each Cartesian quadrant shown in orange. Bottom: Same as above between sorted BCL11B WT vs. BCL11B cKO DN3 primary thymocytes (n=2; horizontal axis) and *in vitro* differentiated SMARCA4 WT vs. SMARCA4 cKO DN3 thymocytes (n=2; vertical axis). **c,** Fraction of transcriptionally

active jointly SMARCA4-induced BCL11B-induced T_{EFF} loci in DN2-DN3 thymocytes (left; n=2) and of transcriptionally active jointly SMARCA4-induced BCL11B-repressed loci in DN2-DN3 thymocytes (right; n=2). **d,** Volcano plots of differential gene expression between sorted BCL11B WT vs. BCL11B cKO ETP-DN3 primary thymocytes (n=2) across actively transcribed T effector genes. Marginal rugs (blue lines) indicate distribution of values along each axis. **e,** MA plot depicting the $\log_2$ fold-change of normalized ATAC-seq fragments at T_{EFF} loci between sorted BCL11B WT vs. BCL11B cKO DN2-DN3 primary thymocytes (n=2). Statistically significant differentially expressed peaks (Benjamini-Hochberg-corrected FDR < 0.1) are highlighted in orange. **f,** Representative aggregate histograms of ATAC-seq at jointly SMARCA4-induced BCL11B-induced vs. jointly SMARCA4-induced BCL11B-repressed T_{EFF} loci in sorted BCL11B WT primary thymocytes (1 of n=2). **g,** Bar plots representing the fraction of jointly SMARCA4-induced BCL11B-induced vs. jointly SMARCA4-induced BCL11B-repressed T_{EFF} loci in DN2-DN3 thymocytes that are also accessible in NK cells and ILCs (merged ILC1, ILC2, ILC3)[11]. **h,** Reciprocal co-immunoprecipitations of IgG, SMARCA4, BCL11B and PBRM1 (columns) from nuclear extracts (1mg/mL) of CCRF-CEM human T cell line and immunoblots of co-immunoprecipitating SMARCA4, PBRM1 and BCL11B (rows). (Input sample, immunoprecipitant (IP), flow-through fraction of non-interacting proteins (FT), molecular weight markers (M)). **i**, Density sedimentation (glycerol gradient; horizontal axis) and immunoblot of SMARCA4, PBRM1 and BCL11B (rows) from nuclear extracts of CCRF-CEM human T cell line. 1mg total extract loaded onto gradient. **j**, Density sedimentations (glycerol gradient; horizontal axes) and immunoblots of SMARCA4, PBRM1 and BCL11B (rows) from untreated nuclear extracts (left) and benzonase-treated nuclear extracts (right) of total thymocytes from WT mice. 1mg total extract loaded onto each gradient. **k,** Reciprocal co-immunoprecipitations of IgG, SMARCA4, BCL11B and PBRM1 (columns) from high-concentration nuclear extracts (10mg/mL) of total thymocytes from wild-type mice and immunoblots of co-immunoprecipitating SMARCA4, PBRM1 and BCL11B (rows). (Input sample, immunoprecipitant (IP), flow-through fraction of non-interacting proteins (FT), molecular weight markers (M)). **l,** Representative aggregate histograms of BAF155 occupancy (CUT&RUN) at jointly SMARCA4-induced, BCL11B-induced (left) vs. jointly SMARCA4-induced, BCL11B-repressed (right) T effector loci in sorted BCL11B WT vs. BCL11B cKO primary DN2-DN3 thymocytes (1 of n=2). **m,** Cumulative distribution functions of the $\log_2$ fold-change in RUNX1 occupancy (ChIP-seq[32]) between sorted BCL11B WT and BCL11B cKO primary DN2-DN3 thymocytes at BCL11B-induced, BCL11B-independent and BCL11B-repressed (n=2) T_{EFF} loci. P-values from one-sided Wilcoxon signed-rank tests (using BCL11B-independent distribution as the null) are displayed.

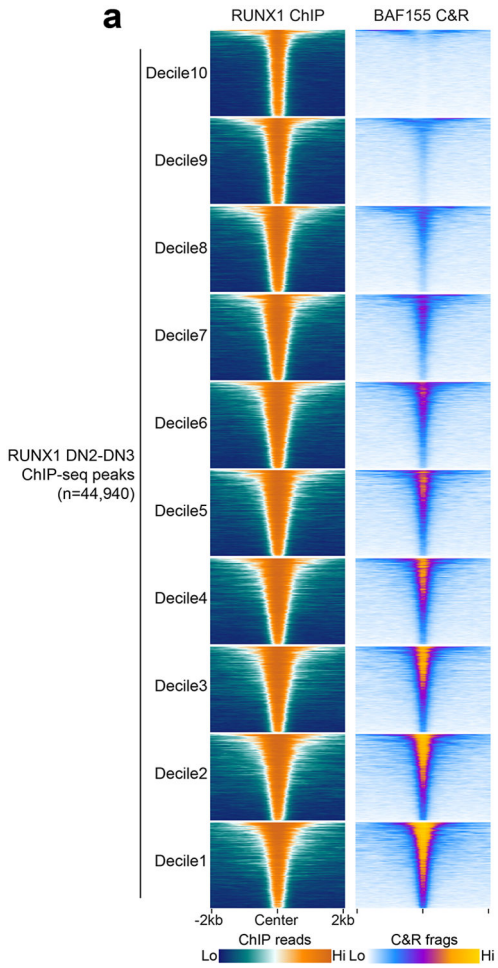

Extended Data Figure 9. mSWI/SNF-associated RUNX1 complexes are a subset of a heterogeneous pool of RUNX1 complexes in the nucleus.

a, Representative heatmaps of RUNX1 occupancy (ChIP-seq[32]) (left; 1 of n=2) and BAF155 occupancy (CUT&RUN) (right; 1 of n = 3) across all RUNX1 ChIP-seq peaks in DN2-DN3 thymocytes partitioned by BAF155 fragment density decile (rows).

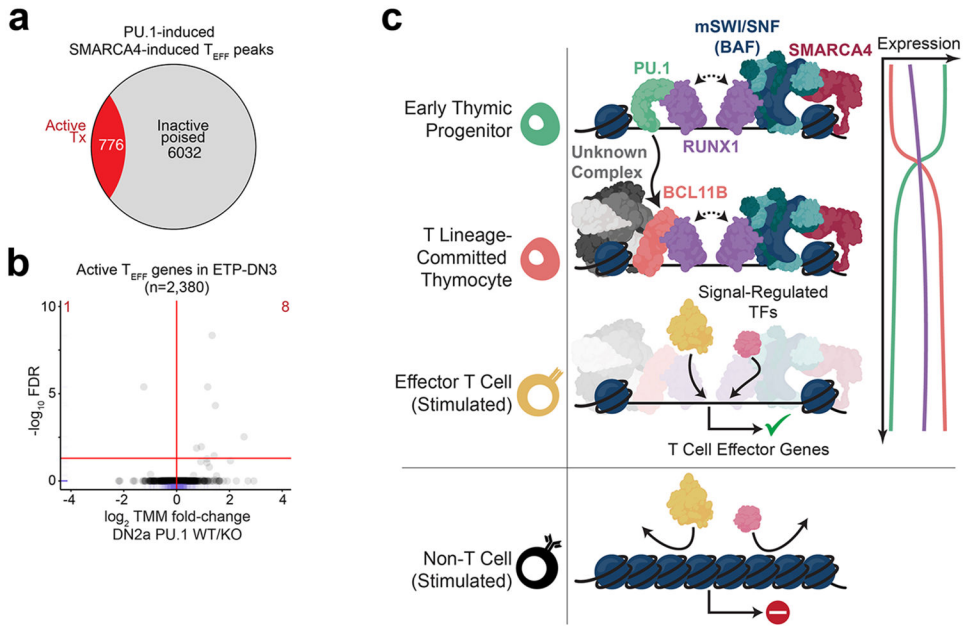

Extended Data Figure 10. Working model of transcription factor relay for specification of T effector potential.

a, Fraction of transcriptionally active jointly SMARCA4-induced, PU.1-induced loci in *in vitro* differentiated DN2a thymocytes (n=3). **b,** Volcano plot of differential gene expression between *in vitro* differentiated PU.1 WT vs. PU.1 cKO DN2a thymocytes (n=2) across actively transcribed T effector genes. Marginal rugs (blue lines) indicate distribution of values along each axis. **c,** Schematic of cooperative transcription factor relay that recruits and maintains mSWI/SNF occupancy at T_{EFF} loci to equip thymocytes for T effector potential.

Supplementary Material

Refer to Web version on PubMed Central for supplementary material.

ACKNOWLEDGMENTS

We are grateful to M. Leid (Oregon State University) for *Bcl11b f/f* mice; P. Liu (NIH/NHGRI) for *Runx1 f/f* mice; J.C. Zúñiga-Pflücker (University of Toronto) for OP9-DL4 cell line; S. Henikoff (Fred Hutchinson Cancer Center) for protein A-MNase; and C. Chang, B. Shin, V. Cismasiu, D. Avram for CUT&RUN troubleshooting. We thank S. Smale, A. Weinmann, C. Kadoch and members of the Koh Lab for critical reading of the manuscript. This work was supported by grants from the National Institute of Health (R35-GM138150, 2UL1TR002389-06, 5UL1TR002389-04 to A.S.K.; CA-163915 to G.R.C., T32-EB009412, T32-AI07090 to N.G.; T32-CA009594 to J.M.; and T32-GM139782 to O.B.); the Howard Hughes Medical Institute (to G.R.C.); and the Chan Zuckerberg Biohub (to W.J.G.). Fellowship support was provided by: The Stamps Scholarship (to A.B.); University of Chicago Women's Board (to C.K.); Stanford Immunology Baker Fellowship and Korea Foundation for Advanced Studies Overseas PhD Scholarship (to Y.K.); JIMB/NIST training program (to B.P.); and The Stanford Genome Training Program (NIH/NHGRI) (to S.K.). Flow cytometry was supported by the University of Chicago Human Disease and Immune Discovery Facility (RRID:SCR_022936), the Cytometry and Antibody Technology Facility (RRID:SCR_017760); and the Stanford Shared FACS Facility (NIH S10RR025518). Genomics sequencing was supported by the University of Chicago Genomics Facility (RRID:SCR_019196), which receives support from the Cancer Center Support Grant (P30-CA014599).

DATA AVAILABILITY

Original raw ATAC-seq and CUT&RUN data have been deposited to the National Center for Biotechnology Information (NCBI) Gene Expression Omnibus, Accession: GSE234331. Additional Gene Expression Omnibus accession numbers for published datasets used in this study include GSE132531, GSE140187, GSE118112, GSE127768, GSE100738, GSE118189, GSE90958, GSE77695, GSE94039, GSE31233, GSE110305, GSE93755, GSE110020, GSE103953, GSE88967, GSE115744, GSE116204, GSE123198, GSE98412, GSE64409, GSE172358 and GSE40463. Raw immunoblot images from Figs. 5a, 5b, 6c, 6d and Extended Data Figs. 8h, 8i, 8j, 8k were deposited to Mendeley at doi:10.17632/zws5pvcyzp.1 and are included in Supplementary Information. All sequencing data was aligned using the mm10 mouse genome assembly.

CODE AVAILABILITY

This study did not generate new code.

REFERENCES

1. Mosmann TR & Coffman RL TH1 and TH2 cells: different patterns of lymphokine secretion lead to different functional properties. Annu Rev Immunol 7, 145–173 (1989). [PubMed: 2523712]
2. Williams MA & Bevan MJ Effector and memory CTL differentiation. Annu Rev Immunol 25, 171–192 (2007). [PubMed: 17129182]
3. van Panhuys N, Klauschen F & Germain RN T-cell-receptor-dependent signal intensity dominantly controls CD4(+) T cell polarization In Vivo. Immunity 41, 63–74 (2014). [PubMed: 24981853]
4. Fazilleau N, McHeyzer-Williams LJ, Rosen H & McHeyzer-Williams MG The function of follicular helper T cells is regulated by the strength of T cell antigen receptor binding. Nat Immunol 10, 375–384 (2009). [PubMed: 19252493]
5. Tubo NJ et al. Single naive CD4+ T cells from a diverse repertoire produce different effector cell types during infection. Cell 153, 785–796 (2013). [PubMed: 23663778]
6. Scott-Browne JP et al. Dynamic Changes in Chromatin Accessibility Occur in CD8+ T Cells Responding to Viral Infection. Immunity 45, 1327–1340 (2016). [PubMed: 27939672]
7. Zhong Y. et al. Hierarchical regulation of the resting and activated T cell epigenome by major transcription factor families. Nat Immunol 23, 122–134 (2022). [PubMed: 34937932]
8. Shih HY et al. Developmental Acquisition of Regulomes Underlies Innate Lymphoid Cell Functionality. Cell 165, 1120–1133 (2016). [PubMed: 27156451]
9. Pandey S, Kawai T & Akira S Microbial sensing by Toll-like receptors and intracellular nucleic acid sensors. Cold Spring Harbor perspectives in biology 7, a016246 (2014). [PubMed: 25301932]
10. Taniguchi K & Karin M NF-κB, inflammation, immunity and cancer: coming of age. Nature Reviews Immunology 18, 309–324 (2018).
11. Desai DM, Newton ME, Kadlecek T & Weiss A Stimulation of the phosphatidylinositol pathway can induce T-cell activation. Nature 348, 66–69 (1990). [PubMed: 2234059]
12. Calderon D. et al. Landscape of stimulation-responsive chromatin across diverse human immune cells. Nat Genet 51, 1494–1505 (2019). [PubMed: 31570894]
13. Buck MD, Sowell RT, Kaech SM & Pearce EL Metabolic Instruction of Immunity. Cell 169, 570–586 (2017). [PubMed: 28475890]
14. Rothenberg EV & Ward SB A dynamic assembly of diverse transcription factors integrates activation and cell-type information for interleukin 2 gene regulation. Proc Natl Acad Sci U S A 93, 9358–9365 (1996). [PubMed: 8790334]
15. Samstein Robert M. et al. Foxp3 Exploits a Pre-Existent Enhancer Landscape for Regulatory T Cell Lineage Specification. Cell 151, 153–166 (2012). [PubMed: 23021222]

16. Buenrostro JD, Wu B, Chang HY & Greenleaf WJ ATAC-seq: A Method for Assaying Chromatin Accessibility Genome-Wide. Current protocols in molecular biology 109, 21.29.21–29 (2015).
17. Yoshida H. et al. The cis-Regulatory Atlas of the Mouse Immune System. Cell 176, 897–912.e820 (2019). [PubMed: 30686579]
18. Petermann F. et al. The Magnitude of IFN-γ Responses Is Fine-Tuned by DNA Architecture and the Non-coding Transcript of Ifng-as1. Mol Cell 75, 1229–1242.e1225 (2019). [PubMed: 31377117]
19. Choi J. et al. Bcl-6 is the nexus transcription factor of T follicular helper cells via repressor-of-repressor circuits. Nat Immunol 21, 777–789 (2020). [PubMed: 32572238]
20. Hayward SL et al. Environmental cues regulate epigenetic reprogramming of airway-resident memory CD8(+) T cells. Nat Immunol 21, 309–320 (2020). [PubMed: 31953534]
21. Qiu R. et al. Inhibition of Glycolysis in Pathogenic T(H)17 Cells through Targeting a miR −21-Peli1-c-Rel Pathway Prevents Autoimmunity. J Immunol 204, 3160–3170 (2020). [PubMed: 32414810]
22. Lio CJ et al. TET enzymes augment activation-induced deaminase (AID) expression via 5-hydroxymethylcytosine modifications at the Aicda superenhancer. Sci Immunol 4 (2019).
23. Open-source ImmGen: mononuclear phagocytes. Nat Immunol 17, 741 (2016). [PubMed: 27327993]
24. Miller EL et al. TOP2 synergizes with BAF chromatin remodeling for both resolution and formation of facultative heterochromatin. Nat Struct Mol Biol **advance online publication** (2017).**advance online publication**
25. Gallo EM, Ho L, Winslow MM, Staton TL & Crabtree GR Selective role of calcineurin in haematopoiesis and lymphopoiesis. EMBO reports 9, 1141–1148 (2008). [PubMed: 18818667]
26. Isoda T. et al. Non-coding Transcription Instructs Chromatin Folding and Compartmentalization to Dictate Enhancer-Promoter Communication and T Cell Fate. Cell 171, 103–119.e118 (2017). [PubMed: 28938112]
27. Hosokawa H. et al. Bcl11b sets pro-T cell fate by site-specific cofactor recruitment and by repressing Id2 and Zbtb16. Nat Immunol 19, 1427–1440 (2018). [PubMed: 30374131]
28. Calo E & Wysocka J Modification of Enhancer Chromatin: What, How, and Why? Molecular Cell 49, 825–837 (2013). [PubMed: 23473601]
29. Buecker C & Wysocka J Enhancers as information integration hubs in development: lessons from genomics. Trends in Genetics 28, 276–284 (2012). [PubMed: 22487374]
30. Pham D. et al. Batf stabilizes Th17 cell development via impaired Stat5 recruitment of Ets1-Runx1 complexes. The EMBO journal 42, e109803 (2023). [PubMed: 36917143]
31. Carr TM, Wheaton JD, Houtz GM & Ciofani M JunB promotes Th17 cell identity and restrains alternative CD4(+) T-cell programs during inflammation. Nature communications 8, 301 (2017).
32. Martinez GJ et al. The transcription factor NFAT promotes exhaustion of activated $CD8^+$ T cells. Immunity 42, 265–278 (2015). [PubMed: 25680272]
33. Tsao HW et al. Batf-mediated epigenetic control of effector CD8(+) T cell differentiation. Sci Immunol 7, eabi4919 (2022). [PubMed: 35179948]
34. Oh H. et al. An NF-κB Transcription-Factor-Dependent Lineage-Specific Transcriptional Program Promotes Regulatory T Cell Identity and Function. Immunity 47, 450–465.e455 (2017). [PubMed: 28889947]
35. Fang D. et al. Differential regulation of transcription factor T-bet induction during NK cell development and T helper-1 cell differentiation. Immunity 55, 639–655.e637 (2022). [PubMed: 35381213]
36. Hsieh T. et al. JunB Is Critical for Survival of T Helper Cells. Frontiers in immunology 13, 901030 (2022). [PubMed: 35837408]
37. Vahedi G. et al. STATs shape the active enhancer landscape of T cell populations. Cell 151, 981–993 (2012). [PubMed: 23178119]
38. Kingston RE & Tamkun JW Transcriptional regulation by trithorax-group proteins. Cold Spring Harbor perspectives in biology 6, a019349 (2014). [PubMed: 25274705]

39. Zhang JA, Mortazavi A, Williams BA, Wold BJ & Rothenberg EV Dynamic transformations of genome-wide epigenetic marking and transcriptional control establish T cell identity. Cell 149, 467–482 (2012). [PubMed: 22500808]
40. Schmitt TM & Zúñiga-Pflücker JC Induction of T cell development from hematopoietic progenitor cells by delta-like-1 in vitro. Immunity 17, 749–756 (2002). [PubMed: 12479821]
41. Skene PJ & Henikoff S An efficient targeted nuclease strategy for high-resolution mapping of DNA binding sites. eLife 6 (2017).
42. Shin B et al. Runx1 and Runx3 drive progenitor to T-lineage transcriptome conversion in mouse T cell commitment via dynamic genomic site switching. Proc Natl Acad Sci U S A 118 (2021).
43. Ho L & Crabtree GR Chromatin remodelling during development. Nature 463, 474–484 (2010). [PubMed: 20110991]
44. Ikawa T. et al. An essential developmental checkpoint for production of the T cell lineage. Science 329, 93–96 (2010). [PubMed: 20595615]
45. Li L, Leid M & Rothenberg EV An early T cell lineage commitment checkpoint dependent on the transcription factor Bcl11b. Science 329, 89–93 (2010). [PubMed: 20595614]
46. Li P et al. Reprogramming of T cells to natural killer-like cells upon Bcl11b deletion. Science 329, 85–89 (2010). [PubMed: 20538915]
47. Kadoch C. et al. Proteomic and bioinformatic analysis of mammalian SWI/SNF complexes identifies extensive roles in human malignancy. Nat Genet 45, 592–601 (2013). [PubMed: 23644491]
48. Hosokawa H. et al. Bcl11b sets pro-T cell fate by site-specific cofactor recruitment and by repressing Id2 and Zbtb16. Nat Immunol 19, 1427–1440 (2018). [PubMed: 30374131]
49. Califano D. et al. Transcription Factor Bcl11b Controls Identity and Function of Mature Type 2 Innate Lymphoid Cells. Immunity 43, 354–368 (2015). [PubMed: 26231117]
50. Voss TC et al. Dynamic exchange at regulatory elements during chromatin remodeling underlies assisted loading mechanism. Cell 146, 544–554 (2011). [PubMed: 21835447]
51. Miller JA & Widom J Collaborative Competition Mechanism for Gene Activation In Vivo. Molecular and cellular biology 23, 1623–1632 (2003). [PubMed: 12588982]
52. Bakshi R. et al. The human SWI/SNF complex associates with RUNX1 to control transcription of hematopoietic target genes. Journal of Cellular Physiology 225, 569–576 (2010). [PubMed: 20506188]
53. Hosokawa H. et al. Transcription Factor PU.1 Represses and Activates Gene Expression in Early T Cells by Redirecting Partner Transcription Factor Binding. Immunity 48, 1119–1134.e1117 (2018). [PubMed: 29924977]
54. Minderjahn J. et al. Mechanisms governing the pioneering and redistribution capabilities of the non-classical pioneer PU.1. Nature communications 11, 402 (2020).
55. Wu J. et al. Requisite Chromatin Remodeling for Myeloid and Erythroid Lineage Differentiation from Erythromyeloid Progenitors. Cell Rep 33, 108395 (2020). [PubMed: 33207205]
56. Shin B, Zhou W, Wang J, Gao F & Rothenberg EV Runx factors launch T cell and innate lymphoid programs via direct and gene network-based mechanisms. Nature Immunology 24, 1458–1472 (2023). [PubMed: 37563311]

METHODS REFERENCES

57. Sumi-Ichinose C, Ichinose H, Metzger D & Chambon P SNF2beta-BRG1 is essential for the viability of F9 murine embryonal carcinoma cells. Mol.Cell Biol 17, 5976–5986 (1997). [PubMed: 9315656]
58. Golonzhka O. et al. Dual role of COUP-TF-interacting protein 2 in epidermal homeostasis and permeability barrier formation. J Invest Dermatol 129, 1459–1470 (2009). [PubMed: 19092943]
59. Taniuchi I. et al. Differential requirements for Runx proteins in CD4 repression and epigenetic silencing during T lymphocyte development. Cell 111, 621–633 (2002). [PubMed: 12464175]

60. Holmes R & Zuniga-Pflucker JC The OP9-DL1 system: generation of T-lymphocytes from embryonic or hematopoietic stem cells in vitro. Cold Spring Harbor protocols 2009, pdb.prot5156 (2009).

61. Buenrostro JD, Giresi PG, Zaba LC, Chang HY & Greenleaf WJ Transposition of native chromatin for fast and sensitive epigenomic profiling of open chromatin, DNA-binding proteins and nucleosome position. Nat Methods 10, 1213–1218 (2013). [PubMed: 24097267]

62. Zhou W, Gao F, Romero-Wolf M, Jo S & Rothenberg EV Single-cell deletion analyses show control of pro-T cell developmental speed and pathways by Tcf7, Spi1, Gata3, Bcl11a, Erg, and Bcl11b. Sci Immunol 7, eabm1920 (2022). [PubMed: 35594339]

63. Romero-Wolf M. et al. Notch2 complements Notch1 to mediate inductive signaling that initiates early T cell development. The Journal of cell biology 219 (2020).

64. Hosokawa H. et al. Stage-specific action of Runx1 and GATA3 controls silencing of PU.1 expression in mouse pro-T cells. J Exp Med 218 (2021).

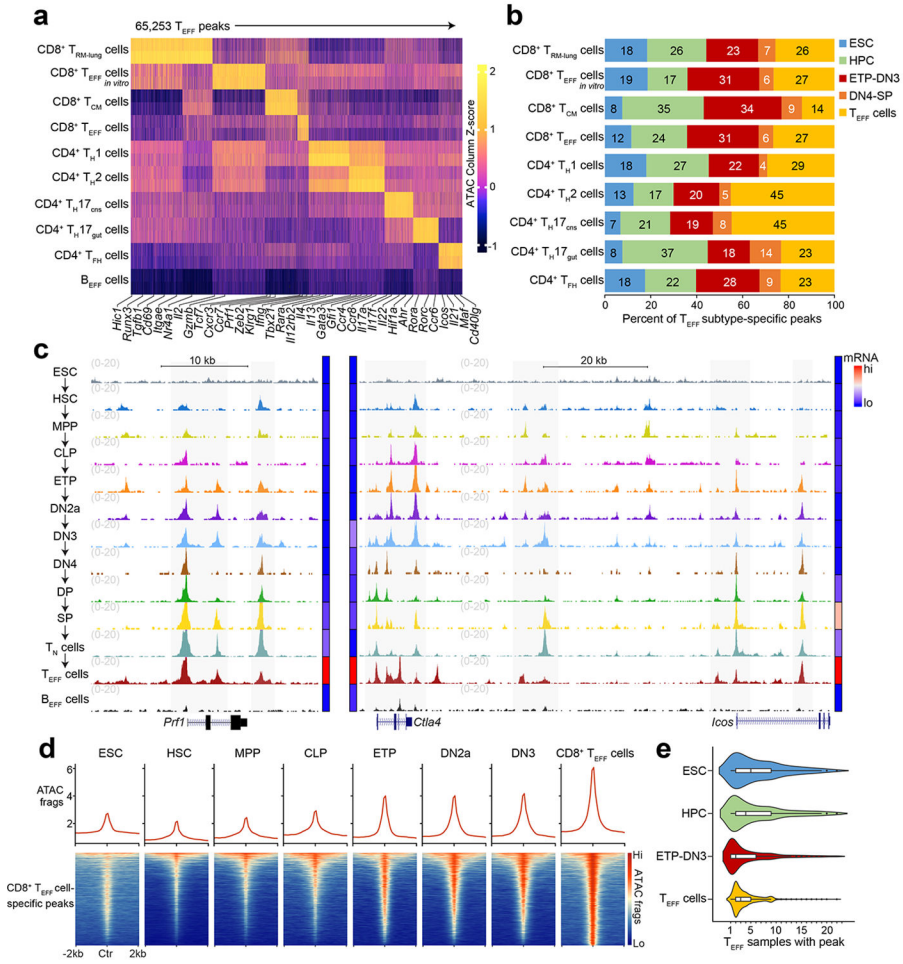

Figure 1. Chromatin accessibility at many T effector loci is established prior to TCR expression.

a, Heatmap of Z scores of TSS-normalized ATAC-seq fragments across the k-means clustered (k=9) T effector loci (hereafter T_{EFF} loci) in lung $CD8^+IV^-CD44^+$influenza-d35-specific tissue-resident memory $CD8^+$ T cells[20] ($CD8^+$ T_{RM} cells), $CD8^+CD19^-\gamma\delta TCR^-TCR\beta^{hi}CD44^{lo}CD62L^{hi}$ naïve T cells (T_N cells) *in vitro* activated with CD3ε/CD28 Abs ($CD8^+$ T_{EFF} *in vitro* cells), $CD8^+KLRG1^+CD127^-$LCMV-d7-specific terminal effector T cells[17] ($CD8^+$ T_{EFF} cells), $CD8^+CD44^+CD62L^+$LCMV-d180-specific central memory T cells[17] ($CD8^+$ T_{CM} cells), IL-12/IL-4-Ab-treated $CD4^+$ T_N cells[18] (T_H1 cells), IL-4/IFNγ-Ab-treated $CD4^+$ T_N cells[18] (T_H2 cells), IL-17A-GFP$^+$CD4$^+$TCRβ$^+$ T cells[21] from ileum (T_H17_{gut} cells) or inflamed brain/spinal cord (T_H17_{CNS} cells), $CD4^+CXCR5^+SLAM^{lo/int}$ T cells[19] (T_{FH} cells) and IL-4/LPS-treated B cells (B_{EFF} cells)[22] (n=2 each). **b,** Bar plots showing the developmental stages at which T_{EFF} loci specific to indicated T_{EFF} cell subtypes in **a** first became accessible. Serum+LIF-maintained embryonic stem cells[24] (ESCs), hematopoietic progenitor cells (HPCs) as aggregate of $CD127^-cKit^{hi}Sca\text{-}1^+Flt3^-$ hematopoietic stem cells[8] (HSCs), $CD127^-cKit^{hi}Sca\text{-}1^+Flt3^+$ multipotent progenitors[8] (MPPs) and $CD127^+cKit^{hi}Sca\text{-}1^+Flt3^+$ common lymphoid progenitors[8] (CLPs); ETP-DN3 thymocytes as aggregate of $\gamma\delta TCR^-CD11b^-CD11c^-CD19^-B220^-NK\text{-}1.1^-Gr\text{-}1^-TER\text{-}119^-$

(Lin$^-$) cKit^{hi}CD25$^-$CD4$^-$CD8$^-$ (ETPs), and Lin$^-$cKit^{hi}CD25^{hi}CD4$^-$CD8$^-$ (DN2a) and Lin$^-$c-Kit$^-$CD25^{hi}CD4$^-$CD8$^-$ (DN3); DN4-SP thymocytes as aggregate of Lin$^-$c-Kit$^-$CD25$^-$CD44$^-$CD4$^-$CD8$^-$ (DN4), Lin$^-$CD4$^+$CD8$^+$TCRβ^{lo}CD69$^-$ (DP), Lin$^-$CD4$^+$CD8$^-$TCRβ^{hi} (CD4SP) and Lin$^-$CD4$^-$CD8$^+$TCRβ^{hi} (CD8SP) and indicated T_{EFF} cells. **c,** Representative genome browser of ATAC-seq (1 of n=2 each) in ESC, HSC, MPP, CLP, ETP, DN2a, DN3, DN4, DP, CD8 SP, T_N, T_{EFF}, B_{EFF} at *Prf1* (T_{EFF}=CD8$^+$ T_{EFF} *in vitro*), *Ctla4* and *Icos* (T_{EFF}=T_{FH}). Adjoined bars indicate transcripts-per-million (TPM) from RNA-seq in each cell type of indicated gene. **d,** Representative aggregate histograms (top) and heatmaps (bottom) (1 of n=2) of ATAC-seq fragments of ESC, HSC, MPP, CLP, ETP, DN2a, DN3 and CD8$^+$ T_{EFF} *in vitro* that intersect open chromatin regions specific to CD8$^+$ T_{EFF} *in vitro*. **e,** Violin plots (boxes represent 1st, median and 3rd quartiles; whiskers represent median +/− 1.5 interquartile range) representing the number of overlap between each ATAC-seq peak (columns in **a**) and all T effector ATAC-seq profiles (rows in **a**), grouped by the developmental windows (ESC, HPC, ETP-DN3 and respective T_{EFF} cells) during which the ATAC-seq peak first became accessible.

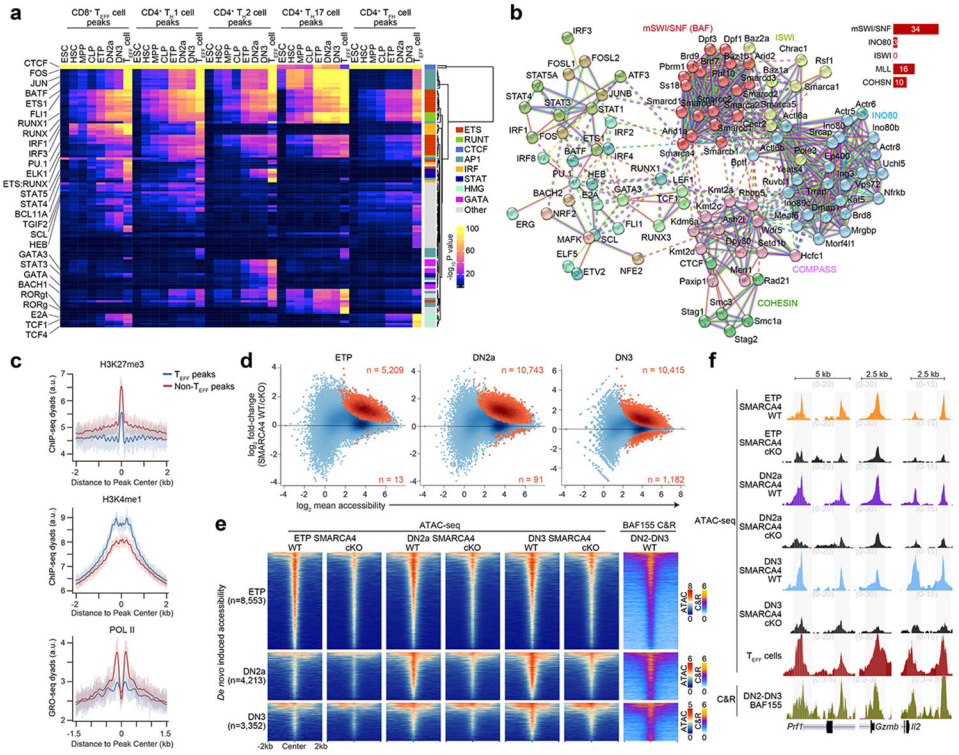

Figure 2. Early poising of T_{EFF} loci is dependent on the mSWI/SNF ATPase SMARCA4.

a, Heatmaps depicting $-\log_{10}$ P values of transcription factor motif enrichments for the top 100 motifs with family classification (vertical axis) within each of the CD8+ T_{EFF}-, $CD4^+$ T_H1-, $CD4^+$ T_H2-, $CD4^+$ T_H17- and $CD4^+$ T_{FH}-specific peaks that were accessible in ESC, HSC, MPP, CLP, ETP, DN2a, DN3 and respective T_{EFF} type (n=2 each) developmental stages (horizontal axis). **b,** STRING high-confidence protein-protein interaction network generated from top decile (n=44) transcription factors from **a** and known subunits of mSWI/SNF, ISWI, INO80, COMPASS and Cohesin complexes. Node colors indicate MCL cluster assignment with dotted lines indicating inter-cluster interactions. Red lines indicate experimentally determined interactions; blue lines indicate curated databases-determined interaction; green lines indicate text mining-determined interactions. **c,** Representative aggregate histograms of H3K27me3[39] (top; 1 of n=2) or H3K4me1[26] (middle; 1 of n=2) ChIP-seq dyads or GRO-seq dyads[26] (bottom; 1 of n=2) over T_{EFF} peaks and non-T_{EFF} peaks in wild-type mouse DN2-DN3 thymocytes. **d,** MA plots depicting the $\log_2$ fold-change of normalized ATAC-seq fragments at T_{EFF} loci between SMARCA4 WT and SMARCA4 cKO ETP (n=3), DN2a (n=3) and DN3 (n=2) thymocytes. Statistically significant differentially expressed peaks (Benjamini-Hochberg-corrected FDR < 0.1) are highlighted in orange. **e,** Representative heatmaps of ATAC-seq fragments from *in vitro* differentiated SMARCA4 WT and SMARCA4 cKO ETP (1 of n=3), DN2a (1 of n=3) and DN3 (1 of n=2) thymocytes and BAF155 occupancy (CUT&RUN) from *in vitro* differentiated SMARCA4 WT DN2-DN3 thymocytes (1 of n=3) that intersect T_{EFF} loci that first become accessible in ETP (top), DN2a (middle) and DN3 (bottom) thymocytes. **f,** Representative genome browser of ATAC-seq fragments from *in vitro* differentiated SMARCA4 WT and SMARCA4 cKO ETP (1 of n=3), DN2a (1 of n=3), DN3 (1 of n=2)

thymocytes and CD8$^+$ T_{EFF} *in vitro* (1 of n=2) (top) and BAF155 occupancy (1 of n=3) (bottom) in *in vitro* differentiated SMARCA4 WT DN2-DN3 thymocytes at *Prf1*, *Gzmb* and *Il2* loci.

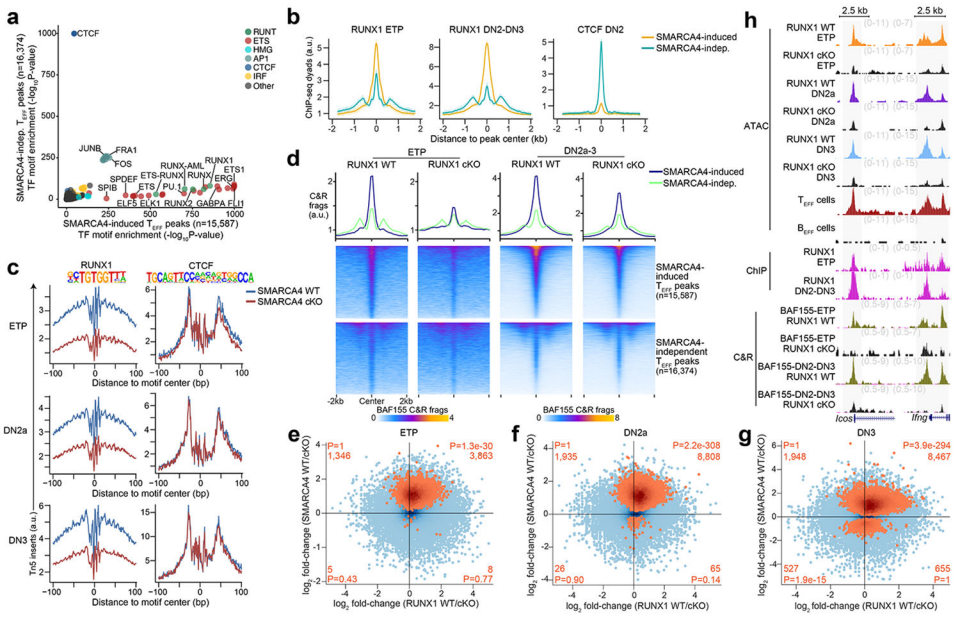

Figure 3. RUNX1 partners with mSWI/SNF to poise T_{EFF} loci in early T cell development.

a, Scatter plot of $-\log_{10}$ P values of transcription factor motif enrichment within SMARCA4-induced (horizontal axis) vs. SMARCA4-independent (vertical axis) T_{EFF} loci from ETP, DN2a or DN3 thymocytes. **b,** Representative aggregate histograms of RUNX1 occupancy (ChIP-seq) in ETPs[42] (left), DN2-DN3 thymocytes[27] (middle) and CTCF occupancy[26] (ChIP-seq) in DN2-DN3 thymocytes at SMARCA4-induced (orange) vs. SMARCA4-independent (cyan) T_{EFF} loci (1 of n=2 for each). **c,** Representative transcription factor footprints (i.e. ATAC-seq inserts near motifs) within T_{EFF} loci centered on RUNX1 and CTCF transcription factor motifs in *in vitro* differentiated SMARCA4 WT vs. SMARCA4 cKO ETP (top; 1 of n=3), DN2a (middle; 1 of n=3) and DN3 (bottom; 1 of n=2) thymocytes. **d,** Representative aggregate histograms and heatmaps of BAF155 occupancy (CUT&RUN) in *in vitro* differentiated RUNX1 WT vs. RUNX1 cKO ETPs (left; 1 of n=2) and DN2-DN3 thymocytes (right; 1 of n=2) over SMARCA4-induced (top heatmaps) or SMARCA4-independent (bottom heatmaps) T_{EFF} loci. **e-g,** Scatter plots depicting the $\log_2$ fold-change of normalized ATAC-seq fragments at T_{EFF} loci between *in vitro* differentiated RUNX1 WT vs. RUNX1 cKO ETPs (n=2; horizontal axis) and *in vitro* differentiated SMARCA4 WT vs. SMARCA4 cKO ETPs (n=3; vertical axis) (**e**); *in vitro* differentiated RUNX1 WT vs. RUNX1 cKO DN2a thymocytes (n=2; horizontal axis) and *in vitro* differentiated SMARCA4 WT vs. SMARCA4 cKO DN2a thymocytes (n=3; vertical axis) (**f**); and *in vitro* differentiated RUNX1 WT vs. RUNX1 cKO DN3 thymocytes (n=2; horizontal axis) and *in vitro* differentiated SMARCA4 WT vs. SMARCA4 cKO DN3 thymocytes (n=2; vertical axis) (**g**). SMARCA4-induced T_{EFF} loci (Benjamini-Hochberg-corrected FDR < 0.1) peaks at each stage are highlighted in orange. Number and statistical enrichment of SMARCA4-induced T_{EFF} loci (determined by one-sided Fisher's exact test) within each Cartesian quadrant shown in orange. **h,** Representative genome browser of ATAC-seq in *in vitro* differentiated RUNX1 WT vs. RUNX1 cKO ETP, DN2a and DN3 thymocytes (1 of n=2 each), T_{EFF} cells and B_{EFF} cells (1 of n=2), RUNX1 occupancy (ChIP-seq) in ETP[42] and DN2-DN3[27] thymocytes (1 of n=2 each) and BAF155 occupancy

in *in vitro* differentiated RUNX1 WT vs. RUNX1 cKO ETP and DN2-DN3 thymocytes (1 of n=2 each) at *Icos* (T_{EFF}=T_{FH}) and *Ifng* (T_{EFF}=T_H1) loci.

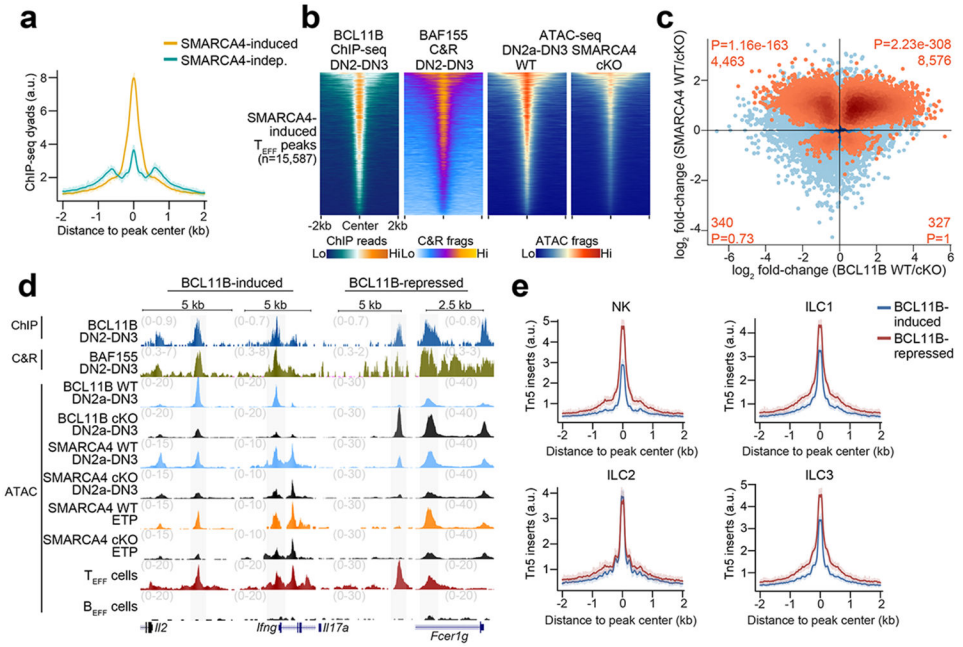

Figure 4. BCL11B maintains chromatin accessibility at SMARCA4-induced T_{EFF} loci.

a, Representative aggregate histograms (1 of n=2) of BCL11B occupancy (ChIP-seq[27]) in WT DN2-DN3 thymocytes over SMARCA4-induced vs. SMARCA4-independent T_{EFF} loci. **b,** Representative heatmaps of BCL11B occupancy (ChIP-seq[27]; 1 of n=2), BAF155 occupancy (CUT&RUN; 1 of n=3) and ATAC-seq (1 of n=2; right) in *in vitro* differentiated SMARCA4 WT vs. SMARCA4 cKO thymocytes intersecting SMARCA4-induced T_{EFF} loci in DN2-DN3 thymocytes. **c,** Scatter plot depicting the $\log_2$ fold-change of normalized ATAC-seq fragments at T_{EFF} loci between sorted BCL11B WT vs. BCL11B cKO DN2-DN3 primary thymocytes (n=2; horizontal axis) and *in vitro* differentiated SMARCA4 WT vs. SMARCA4 cKO DN2-DN3 thymocytes (n=2; vertical axis). SMARCA4-induced T_{EFF} loci (Benjamini-Hochberg-corrected FDR < 0.1) peaks highlighted in orange. Number and statistical enrichment of SMARCA4-induced T_{EFF} loci (determined by one-sided Fisher's exact test) within each Cartesian quadrant shown in orange. **d,** Representative genome browser of BCL11B occupancy (ChIP-seq[27]; 1 of n=2) BAF155 occupancy (CUT&RUN; 1 of n=3) occupancy in DN2-DN3 thymocytes and ATAC-seq in sorted BCL11B WT vs. BCL11B cKO DN2-DN3 primary thymocytes (1 of n=2), *in vitro* differentiated SMARCA4 WT vs. SMARCA4 cKO DN2-DN3 thymocytes, *in vitro* differentiated SMARCA4 WT vs. SMARCA4 cKO ETPs, T_{EFF} cells (1 of n=2) and B_{EFF} cells (1 of n=2) at *Il2, Ifng* (BCL11B-induced, T_{EFF}=T_H1), *Il17a* (T_{EFF}=T_H17) and *Fcer1g* (T_{EFF}=$CD8^+$ T_{RM}) (BCL11B-repressed) loci. **e,** Representative (1 of n=2 for each) aggregate histograms of ATAC-seq inserts over BCL11B-induced and BCL11B-repressed SMARCA4-induced T_{EFF} loci in $CD19^-CD3\varepsilon^-NKp46^+DX5^+TRAIL^-$ natural killer[8] (NK); $CD19^-CD3\varepsilon^-NKp46^+DX5^-TRAIL^+$ (ILC1[8]) $CD3\varepsilon^-CD19^-NKp46^-CD127^+KLRG1^+$ (ILC2[8]) and pooled $CD3\varepsilon^-CD19^-NKp46^-CD127^+KLRG1^-CD4^+$ and $CD3\varepsilon^-CD19^-NKp46^+CD127^+NK1.1^+$ (ILC3[8]).

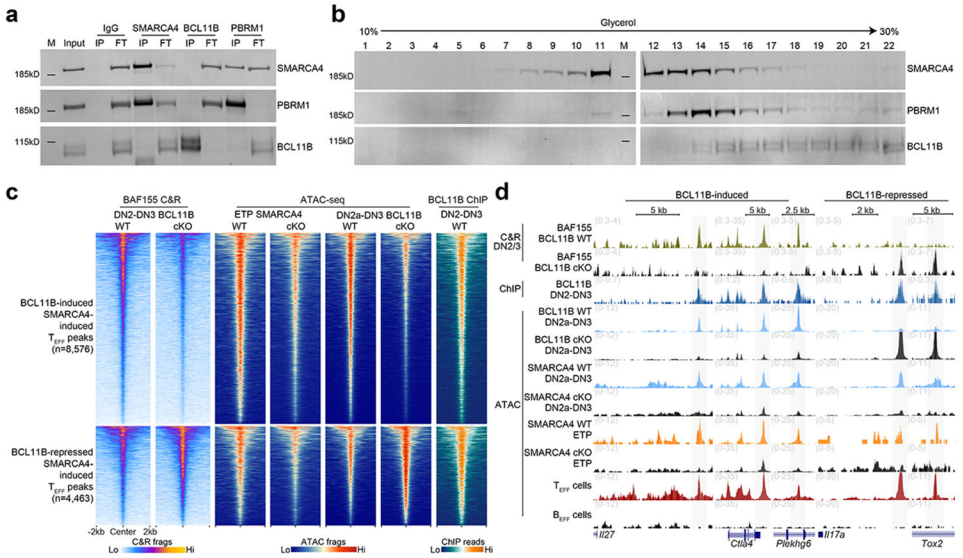

Figure 5. BCL11B maintains mSWI/SNF occupancy at T_{EFF} loci via indirect cooperativity.

a, Reciprocal co-immunoprecipitations of IgG, SMARCA4, BCL11B and PBRM1 (columns) from nuclear extracts (1mg/mL) of total thymocytes from wild-type mice and immunoblots of co-immunoprecipitating SMARCA4, PBRM1 and BCL11B (rows). (Input sample, immunoprecipitant (IP), flow-through fraction of non-interacting proteins (FT), molecular weight markers (M)). **b,** Density sedimentation (glycerol gradient; horizontal axis) and immunoblot of SMARCA4, PBRM1 and BCL11B (rows) from nuclear extracts of total thymocytes from wild-type mice. 1mg total extract loaded onto gradient. **c,** Representative heatmaps of BAF155 CUT&RUN in sorted BCL11B WT vs. BCL11B cKO DN2-DN3 primary thymocytes (1 of n=3), ATAC-seq in *in vitro* differentiated SMARCA4 WT vs. SMARCA4 cKO ETPs (1 of n=3), sorted BCL11B WT vs. BCL11B cKO DN2-DN3 primary thymocytes (1 of n=2) and BCL11B occupancy (ChIP-seq[27]) in DN2-DN3 thymocytes (1 of n=2) intersecting jointly SMARCA4-induced, BCL11B-induced (top) and jointly SMARCA4-induced, BCL11b-repressed (bottom) T_{EFF} loci. **d,** Representative genome browser of BAF155 CUT&RUN in sorted BCL11B WT vs. BCL11B cKO DN2-DN3 primary thymocytes (1 of n=3), BCL11B occupancy (ChIP-seq[27]) in DN2-DN3 thymocytes (1 of n=2), ATAC-seq in sorted BCL11B WT vs. BCL11B cKO primary DN2-DN3 thymocytes (1 of n=2), *in vitro* differentiated SMARCA4 WT vs. SMARCA4 cKO DN2-DN3 thymocytes (1 of n=2), *in vitro* differentiated SMARCA4 WT vs. SMARCA4 cKO DN2-DN3 thymocytes (1 of n=2), T_{EFF} cells (1 of n=2) and B_{EFF} cells (1 of n=2) at *Il27* (T_{EFF}=T_{H2}) , *Ctla4* (T_{EFF}= $CD8^+$ T_{RM}), *Plekhg6* (T_{EFF}=$CD8^+$ T_{EFF} *in vitro*) (SMARCA4-induced, BCL11B-induced; left), *Il17a* (T_{EFF}=T_{H17}) and *Tox2* (T_{EFF}=T_{FH}) (SMARCA4-induced, BCL11B-repressed; right) loci.

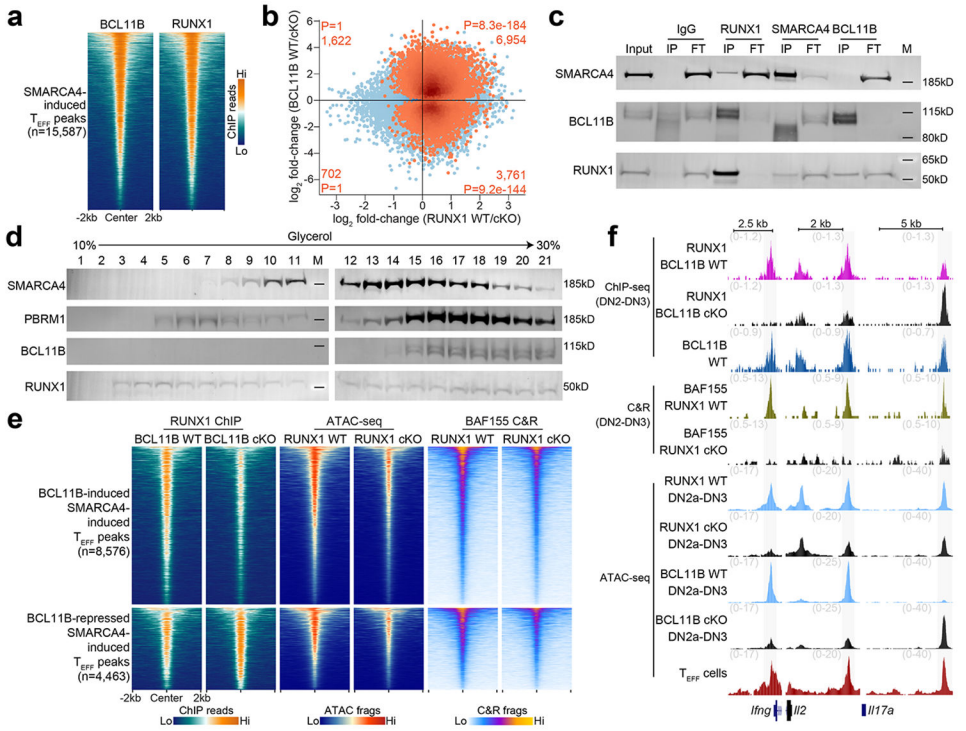

Figure 6. BCL11B and RUNX1 cooperate to maintain mSWI/SNF at T_{EFF} loci.

a, Representative heatmaps (1 of n=2 each) of BCL11B and RUNX1 occupancy (ChIP-seq[27]) in DN2-DN3 thymocytes over SMARCA4-induced T_{EFF} loci. **b,** Scatter plot depicting the log_2 fold-change of normalized ATAC-seq fragments at T_{EFF} loci between *in vitro* differentiated RUNX1 WT vs. RUNX1 cKO DN2-DN3 thymocytes (n=2; horizontal axis) and sorted BCL11B WT vs. BCL11B cKO DN2-DN3 primary thymocytes (n=2; vertical axis). SMARCA4-induced T_{EFF} loci (Benjamini-Hochberg-corrected FDR < 0.1) peaks highlighted in orange. Number and statistical enrichment of SMARCA4-induced T_{EFF} loci (determined by one-sided Fisher's exact test) within each Cartesian quadrant shown in orange. **c,** Reciprocal co-immunoprecipitations of IgG, RUNX1, SMARCA4 and BCL11B (columns) from nuclear extracts (1mg/mL) of primary murine thymocytes and immunoblots of co-immunoprecipitating SMARCA4, BCL11B and RUNX1 (rows). (Input sample, immunoprecipitant (IP), flow-through fraction of non-interacting proteins (FT), molecular weight markers (M)). **d,** Density sedimentation (glycerol gradient; horizontal axis) and immunoblot of SMARCA4, PBRM1, BCL11B and RUNX1 (rows) from nuclear extracts of total thymocytes from wild-type mice. 1mg total extract loaded onto gradient. **e,** Representative heatmaps of RUNX1 occupancy (ChIP-seq[27]) in BCL11B WT vs. BCL11B cKO DN2-DN3 thymocytes (1 of n=2), ATAC-seq in *in vitro* differentiated RUNX1 WT vs. RUNX1 cKO DN2-DN3 thymocytes (1 of n=2) and BAF155 occupancy (CUT&RUN) in *in vitro* differentiated RUNX1 WT vs. RUNX1 cKO DN2-DN3 thymocytes (1 of n=2) intersecting jointly SMARCA4-induced, BCL11B-induced (top) and jointly SMARCA4-induced, BCL11b-repressed (bottom) T_{EFF} loci. **f,** Representative genome browser of RUNX1 occupancy (ChIP-seq[27]) in BCL11B WT vs BCL11B cKO DN2-DN3 thymocytes (1 of n=2), BCL11B occupancy (ChIP-seq[27]) in wild-type DN2-DN3 thymocytes (1 of n=2), BAF155 occupancy (CUT&RUN) in *in vitro* differentiated RUNX1 WT vs. RUNX1

cKO DN2-DN3 thymocytes (1 of n=2), ATAC-seq in *in vitro* differentiated RUNX1 WT vs. RUNX1 cKO DN2-DN3 thymocytes (1 of n=2), sorted BCL11B WT vs. BCL11B cKO DN2-DN3 primary thymocytes (1 of n=2) and T_{EFF} cells (1 of n=2) at *Ifng* (T_{EFF}=T_H1), *Il2* (T_{EFF}=T_H1) and *Il17a* (T_{EFF}=T_H17) (SMARCA4-induced) loci.

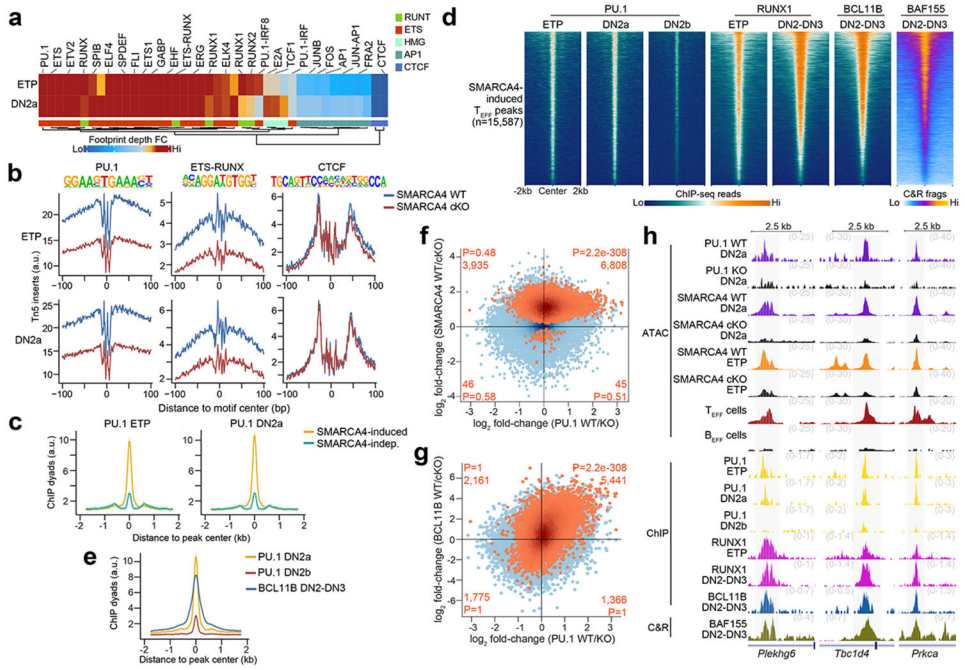

Figure 7. PU.1 partners with RUNX1 to poise T_{EFF} loci at ETP-DN2a stages.

a, Heatmap representing the fold-change in transcription factor footprint depth (flanking accessibility height/footprint base) between *in vitro* differentiated SMARCA4 WT and SMARCA4 cKO ETP and DN2a thymocytes (n=3 each) for previously identified motifs within T_{EFF} loci. **b,** Representative transcription factor footprints (i.e. ATAC-seq inserts near motifs) at T_{EFF} loci centered on PU.1, ETS-RUNX and CTCF motifs in *in vitro* differentiated *SMARCA4* WT vs. SMARCA4 cKO ETP (1 of n=3; top) and DN2a (1 of n=3; bottom) thymocytes. **c**, Representative aggregate histograms of PU.1 occupancy (ChIP-seq[39]) at SMARCA4-induced and SMARCA4-independent T_{EFF} loci in ETPs (left) and DN2a (right) thymocytes (1 of n=2 for each). **d,** Representative heatmaps of PU.1 occupancy (ChIP-seq[39]) in ETP, DN2a and DN2b thymocytes (1 of n=2 each), RUNX1 occupancy (ChIP-seq[27, 42]) in ETP and DN2-DN3 thymocytes (1 of n = 2 each), BCL11B occupancy (ChIP-seq[27]) in DN2-DN3 thymocytes and BAF155 occupancy (CUT&RUN) in *in vitro* differentiated DN2-DN3 thymocytes (1 of n=3) at SMARCA4-induced T_{EFF} loci. **e,** Representative aggregate histograms of PU.1 occupancy (ChIP-seq[39]) in DN2a and DN2b thymocytes and BCL11B occupancy (ChIP-seq[27]) in DN2-DN3 thymocytes at SMARCA4-induced T_{EFF} loci. **f,** Scatter plot depicting the $\log_2$ fold-change of normalized ATAC-seq fragments at T_{EFF} loci between *in vitro* differentiated PU.1 WT vs. PU.1 cKO DN2a thymocytes[53] (n=3; horizontal axis) and *in vitro* differentiated SMARCA4 WT vs. SMARCA4 cKO DN2a thymocytes (n=3; vertical axis). SMARCA4-induced T_{EFF} loci (Benjamini-Hochberg-corrected FDR < 0.1) peaks highlighted in orange. Number and statistical enrichment of SMARCA4-induced T_{EFF} loci (determined by one-sided Fisher's exact test) within each Cartesian quadrant shown in orange. **g,** Scatter plot depicting the $\log_2$ fold-change of normalized ATAC-seq fragments at T_{EFF} loci between *in vitro* differentiated PU.1 WT vs. PU.1 cKO DN2a thymocytes[53] (n=3; horizontal axis) and sorted BCL11B WT vs. BCL11B cKO primary DN2-DN3 thymocytes (n=2; vertical axis). **h,**

Representative genome browser of ATAC-seq in *in vitro* differentiated PU.1 WT vs. PU.1 cKO DN2a thymocytes[53] (1 of n=3), *in vitro* differentiated SMARCA4 WT vs. SMARCA4 cKO DN2a thymocytes (1 of n=3), *in vitro* differentiated SMARCA4 WT vs. SMARCA4 cKO ETPs (1 of n=3), T_{EFF} cells (1 of n = 2) and B_{EFF} cells (1 of n = 2), PU.1 occupancy (ChIP-seq[39]) in wild-type ETP, DN2a and DN2b thymocytes (1 of n=2 each), RUNX1 occupancy (ChIP-seq[27, 42]) in wild-type ETP and DN2-DN3 thymocytes (1 of n=2 each), BCL11B occupancy (ChIP-seq[27]) in wild-type DN2-DN3 thymocytes (1 of n=2) and BAF155 occupancy (CUT&RUN) in wild-type DN2-DN3 thymocytes (1 of n=3) at *Plekhg6* (T_{EFF}= $CD8^+$ T_{EFF} *in vitro*), *Tbc1d4* (T_{EFF}=T_{FH}) *and Prkca* (T_{EFF}=T_H1) loci.